Biophysical Journal
Article

Biophysical Society

Line Tension Controls Liquid-Disordered + Liquid-Ordered Domain Size Transition in Lipid Bilayers

Rebecca D. Usery,[1] Thais A. Enoki,[1] Sanjula P. Wickramasinghe,[1,3] Michael D. Weiner,[2] Wen-Chyan Tsai,[1] Mary B. Kim,[1,4] Shu Wang,[1,5] Thomas L. Torng,[1,6] David G. Ackerman,[1,7] Frederick A. Heberle,[8,9,10] John Katsaras,[9,11] and Gerald W. Feigenson[1,*]

[1]Department of Molecular Biology and Genetics and [2]Department of Physics, Cornell University, Ithaca, New York; [3]Department of Biochemistry and Biophysics at the University of Pennsylvania, Philadelphia, Pennsylvania; [4]Department of Medicine, Baylor College of Medicine, Houston, Texas; [5]Harvard Medical School Library of Integrated Network-based Cellular Signatures Center and Laboratory of Systems Pharmacology, Harvard University, Boston, Massachusetts; [6]Department of Biochemistry, Geisel School of Medicine at Dartmouth College, Hanover, New Hampshire; [7]Scientific Computing, Howard Hughes Medical Institute, Janelia Research Campus, Ashburn, Virginia; [8]Joint Institute for Biological Sciences and [9]Biology and Soft Matter Division, Oak Ridge National Laboratory, Oak Ridge, Tennessee; and [10]The Bredesen Center for Interdisciplinary Research and Graduate Education and [11]Department of Physics and Astronomy, University of Tennessee, Knoxville, Tennessee

ABSTRACT To better understand animal cell plasma membranes, we studied simplified models, namely four-component lipid bilayer mixtures. Here we describe the domain size transition in the region of coexisting liquid-disordered (Ld) + liquid-ordered (Lo) phases. This transition occurs abruptly in composition space with domains increasing in size by two orders of magnitude, from tens of nanometers to microns. We measured the line tension between coexisting Ld and Lo domains close to the domain size transition for a variety of lipid mixtures, finding that in every case the transition occurs at a line tension of ~0.3 pN. A computational model incorporating line tension and dipole repulsion indicated that even small changes in line tension can result in domains growing in size by several orders of magnitude, consistent with experimental observations. We find that other properties of the coexisting Ld and Lo phases do not change significantly in the vicinity of the abrupt domain size transition.

INTRODUCTION

Phase separation in the plasma membrane (PM) would have important implications for the life of a cell. PM properties could then change sharply over a small range of temperature or composition. Any factor that changes the energy per unit length of the interface (i.e., the line tension) could drive changes in interface length and thus domain size. However, the characterization of phase separation in cells has remained elusive due in part to the complexity of the PM: the lipid and protein components are numerous and diverse (1–4), the two bilayer leaflets have very different compositions, and leaflet coupling is poorly understood (5).

The complexity of the PM makes chemically well-defined model membranes a valuable tool for studying principles governing phase coexistence. Phase diagrams are useful for describing the phase regions and the compositional ranges relevant to the PM. As shown in Fig. 1, coexistence of liquid-ordered (Lo) and liquid-disordered (Ld) phases occurs in mixtures of high melting temperature (high-T_m) lipids, low melting temperature (low-T_m) lipids, and cholesterol (chol) (6–9). Domain size in the Ld + Lo region can be tuned by composition alone in mixtures of this type (10). At one extreme, domain growth is limited to the nanometer size scale, as found for 1,2-distearoyl-*sn*-glycero-3-phosphocholine (DSPC)/1-palmitoyl-2-oleoyl-*sn*-glycero-3-phosphocholine (POPC)/chol (11,12). At the other extreme, domain growth is limited only by vesicle size; in these mixtures, domains in giant unilamellar vesicles (GUVs) are many microns in diameter, as with DSPC/1,2-dioleoyl-*sn*-glycero-3-phosphocholine (DOPC)/chol (7). For convenience, we refer to these extreme cases as "nanodomains" and "macrodomains", respectively.

Studies of the four-component mixture DSPC/DOPC/POPC/chol revealed that Ld + Lo domains remain nanoscopic at low DOPC fraction until an abrupt 100-fold size change occurs at higher DOPC fraction (10,13). As we

Submitted December 19, 2016, and accepted for publication February 16, 2017.

*Correspondence: gwf3@cornell.edu

Rebecca D. Usery and Thais A. Enoki contributed equally to this work.

Editor: David Cafiso.

http://dx.doi.org/10.1016/j.bpj.2017.02.033

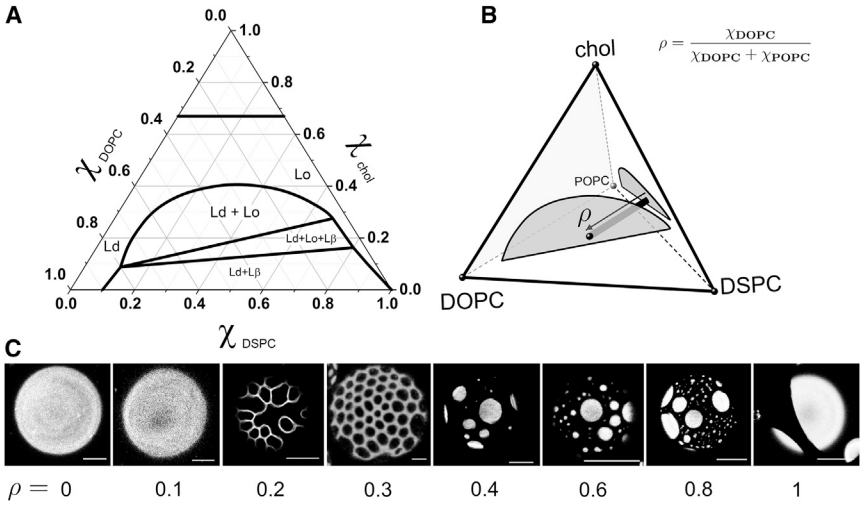

FIGURE 1 Phase diagrams and phase morphologies in four-component mixtures. (*A*) Ternary phase diagram of DSPC/DOPC/Chol at 23°C (9). (*B*) Partial quaternary (*tetrahedral*) phase diagram of DSPC/DOPC/POPC/chol showing the Ld + Lo regions (*shaded*) of DSPC/DOPC/chol (*near face*) and DSPC/POPC/chol (*far-right face*) (9). Sample series referred to in the main text as ρ-trajectories connect a composition on the DSPC/POPC/chol face ($\rho = 0$, nanodomains) to a composition on the DSPC/DOPC/chol face ($\rho = 1$, macrodomains), where ρ represents the ratio of DOPC to total low-T_m lipid (i.e., DOPC + POPC). (*C*) Phase morphologies observed in GUVs along a ρ-trajectory in DSPC/(DOPC+POPC)/chol = 0.39/0.39/0.22: uniform ($\rho < 0.2$); modulated ($0.2 \leq \rho < 0.4$); macroscopic round domains ($\rho \geq 0.4$). Images were collected with a confocal microscope using 0.02 mol % C12:0 DiI. Scale bars, 10 μm.

show here both experimentally and by modeling, increasing line tension drives this nano-to-macro transition. In the course of this size transition, macroscopic patterning of phases or "modulated phase morphology" occurs (10,13). These patterns result from curvature energies that compete with line tension on a round vesicle to break up domains (14–16). The transition from nanometer-scale to micron-scale domains is apparent by imaging giant vesicles: GUVs appear uniform, then patterned, and then with large rounded domains as the compositional range is traversed (10,13).

The abrupt domain size change that occurs with changing mixture composition is the main subject of this work. We show in six different mixtures how line tension increases abruptly when visible domains first appear. In contrast, we find that other properties of Ld and Lo phases do not change sharply even when the domain size does. We propose a model for this abrupt transition in which domain size is determined by a competition between line tension and dipole repulsion. Our results have implications for both how cells could potentially change domain size and what interactions could be responsible for the small size of domains in the PM.

MATERIALS AND METHODS

Materials

Phospholipids were purchased from Avanti Polar Lipids (Alabaster, AL). Purity of phospholipids was found to be better than 99.5% using thin layer chromatography. Briefly, ~20 μg of lipid was spotted on washed and activated Adsorbosil thin-layer chromatography plates (Alltech, Deerfield, IL) and developed in the solvent system chloroform/methanol/water = 65/25/4. Phospholipid concentrations were determined by inorganic phosphate assay (17), with an error < 1% from 10 replicates. Chol was from Nu-Chek Prep (Elysian, MN), and its stock solutions were made at defined concentrations using standard gravimetric procedures. The fluorescent dyes 1,1′-didodecyl-3,3,3′,3′-tetramethylindocarbocyanine perchlorate (C12:0 DiI) and 2-(4,4-difluoro-5,7-dimethyl-4-bora-3a,4a-diaza-s-indacene-3-pentanoyl)-1-hexadecanoyl-*sn*-glycero-3-phosphocholine (BODIPY-PC) were from Invitrogen (Carlsbad, CA). Concentrations were determined by absorption spectroscopy using extinction coefficients of 143,000 M^{-1} cm^{-1} and 91,800 M^{-1} cm^{-1}, respectively. Spin-labeled lipid 1-palmitoyl-2-(16-doxyl stearoyl) phosphatidylcholine (16PC) was a gift from Boris Dzikovski of the National Biomedical Center for Advanced ESR Technology at Cornell University. $F^{4,5}$GWALP23 synthesized according to Gleason et al. (18) was a gift from Roger Koeppe and Denise Greathouse. The peptide was dissolved in 2,2,2-trifluorethanol purchased from Sigma-Aldrich (St. Louis, MO), with the peptide concentration measured by tryptophan absorbance at 280 nm of a 1:500 dilution in methanol, using an extinction coefficient of 5500 M^{-1} cm^{-1}. The buffer used in fluorescence experiments contained 5 mM PIPES (Sigma-Aldrich), 200 mM KCl (Sigma-Aldrich), and 1 mM EDTA (Sigma-Aldrich), at pH 7.0. Sucrose was from Fisher Scientific (Fair Lawn, NJ), and glucose from Teknova (Hollister, CA).

Composition conventions used

Lipid composition and the phase boundaries of each mixture are the key variables in this work, as shown in Fig. 1. We studied lipid mixtures of the type high-T_m lipid/low-T_m phosphatidylcholines (PCs)/chol: *n*-palmitoyl-D-*erythro*-sphingosylphosphorylcholine (pSM)/DOPC/POPC/chol; egg sphingomyelin (eSM)/DOPC/1-stearoyl-2-oleoyl-*sn*-glycero-3-phosphocholine (SOPC)/chol; eSM/DOPC/POPC/chol; DSPC/1,2-diphytanoyl-*sn*-glycero-3-phosphocholine (DPhPC)/1,2-dilauroyl-*sn*-glycero-3-phosphocholine (DLPC)/chol; DSPC/DPhPC/POPC/chol; DSPC/DOPC/POPC/chol; brain sphingomyelin (bSM)/DOPC/POPC/chol; bSM/DOPC/1-palmitoyl-2-linoleoyl-*sn*-glycero-3-phosphocholine (16:0,18:2PC)/chol; bSM/DOPC/SOPC/chol; and bSM/1-stearoyl-2-docosahexaenoyl-*sn*-glycero-3-phosphocholine (SDPC)/POPC/chol.

For molecular dynamics (MD) simulations, we used the mixture 1,2-dipalmitoyl-*sn*-glycero-3-phosphocholine (DPPC)/1,2-dilinoleoyl-*sn*-glycero-3-phosphocholine (DUPC)/1-palmitoyl-2-linoleoyl-*sn*-glycero-3-phosphocholine (PUPC)/chol.

For all mixtures we define a key compositional parameter, the replacement ratio ρ (10,13,16), as the replacement of low-T_m nanodomain-forming PC for low-T_m macrodomain-forming PC. For example, when POPC is replaced by DOPC, ρ = [DOPC]/[DOPC + POPC] (Fig. 1 B), and when SOPC is replaced by DOPC, ρ = [DOPC]/[DOPC + SOPC]. For experiments at a single ρ-value, we describe the lipid composition with the mole fraction of each mixture component, e.g., DSPC/DOPC/POPC/chol = 0.39/0.35/0.04/0.22 for $\rho = 0.1$, and for experiments along ρ, composition is noted as DSPC/DOPC + POPC/chol = 0.39/0.39/0.22.

GUV preparation and phase morphology determination

GUVs were made by electroformation (19) with modifications. Briefly, each sample contained ~300 nmol of a lipid mixture in 200 μL chloroform. A lipid film was created by evenly spreading the chloroform solution on indium tin oxide-coated microscope slides (Delta Technologies, Stillwater, MN) prewarmed on a hotplate with surface temperature measured at ~50°C. After residual solvent was removed under vacuum for 2 h at ~50 mTorr, indium tin oxide slides were sealed with Buna-N O-rings to create a chamber, which was then filled with 100 mM sucrose solution. Films were held above the transition temperature for 2 h in an AC field of 5 Hz, ± 1 Vpp, using a Wavetek Meterman FG2C Function Generator (Meterman, Everett, WA), followed by cooling to 23°C using a Digi-Sense Temperature Controller R/S (Cole Palmer, Vernon Hills, IL). Cooling rates for line tension measurements were varied to control domain size as described in the Supporting Material, and line tension was found to be independent of cooling rate (Fig. S4). GUVs were harvested into 100 mM glucose solution then allowed to settle for 1 h to remove debris before microscopy observations at 23°C. A wide-field microscope, Eclipse Ti (Nikon Instruments, Melville, NY) equipped with a 60×/1.2 NA water immersion objective, was used for all image-based experiments except partition coefficient determination, where an Eclipse C2+ Confocal Microscope (Nikon Instruments) was used. To keep the harvested GUVs intact, an osmolality difference between the sucrose and glucose solutions of <5 mOsmol/kg H_2O was ensured with the use of an osmometer (model No. 5004; Precision Systems, Natick, MA).

GUVs were visualized at 23°C using a wide-field fluorescence microscope. Sample chambers for observation consisted of a No. 1.5 coverslip and traditional microscope slide separated with a silicone spacer (Sigma-Aldrich) of 0.25 mm thickness. Fields of view were selected with bright field illumination before fluorescent images were acquired from emission of C12:0-DiI, which partitions into the Ld phase (20). For phase morphology determination we used this probe at 0.02 mol % of total lipid in the sample to limit light-induced artifacts (21). Images were acquired using a Zyla 5.5 sCMOS camera (Andor Technology, Belfast, UK). For each field of GUVs appearing to be free of defects (e.g., multiple layers or tethers), a series of approximately five 200-ms exposures was taken to capture the surface of GUVs opposite the coverslip. At various values of ρ for the four-component mixtures in this study, the numbers of GUVs with uniform, modulated, and macroscopic patterns were counted. GUVs appearing uniform but with compositions found by spectroscopic methods to have coexisting Lo and Ld phases (8,9,22) were counted as nanoscopic, as in Fig. 1 C ($\rho = 0$ and 0.1). GUVs at intermediate ρ-values exhibiting thin stripes or nonrounded small domains were considered to be modulated, as in Fig. 1 C ($\rho = 0.2$ and 0.3). Macroscopic GUVs were counted as those with large, rounded domains.

Line tension measurements

Line tension was measured using the flicker spectroscopy method of Esposito et al. (23). Briefly, the fluctuation spectrum of a phase domain boundary on a GUV is decomposed into Fourier modes that are related to line tension by

$$\left\langle |u_n|^2 \right\rangle = \frac{2k_BT}{\sigma\pi R_0(n^2-1)}, \quad (1)$$

where n is the mode number, u_n is the mode amplitude, σ is the line tension, R_0 is the radius of a circle yielding the domain area, k_B is the Boltzmann constant, and T is the absolute temperature. For all measurements discussed below, the line tension value was the same whether the fluctuating domain was Ld or Lo and was independent of GUV size or domain size, as shown in more detail in Fig. S5. Additional details of the microscope setup, cooling methods, analysis methodology, and line tension controls are in the Supporting Material.

Bending energy measurements

Bending moduli were measured by fluctuation analysis of GUVs. Fluctuations at the GUV equator were observed by phase contrast microscopy (Fig. S8 *A*). Fluctuation spectra obtained from GUV contours were used to calculate the bending modulus through the relationship

$$\left\langle |u(q)|^2 \right\rangle = \frac{k_BT}{\kappa q^4 + \sigma q^2}, \quad (2)$$

where $u(q)$ is the displacement normal to the membrane, $q = (qx, qy)$ is the wave vector corresponding to the displacement, k_B is the Boltzmann constant, T is the absolute temperature, κ is the bending modulus, and σ is membrane tension. Tension was determined as in Pécréaux et al. (24), and the bending modulus calculated as in Gracià et al. (25). Additional information on measurement methods is provided in the Supporting Material.

The bending moduli of the coexisting phases were determined by measuring single-phase GUVs at the Ld and Lo tieline endpoint compositions at various values of ρ for DSPC/DOPC/POPC/chol. Tieline endpoint compositions near the lower boundary of the Ld + Lo region were taken from Konyakhina et al. (9) and are provided in Table S1.

Partition coefficient (K_p) measurements

Determination of 16PC K_p *from electron spin resonance spectra*

One hundred eleven samples were prepared along a ρ-trajectory of DSPC/DOPC + POPC/chol = 0.39/0.39/0.22 from $\rho = 0$ to 1, with all samples having coexisting Ld + Lo phases. Lipid stock solutions were combined with 0.3 mol % of the spin-labeled lipid 16PC. Chloroform was then removed under nitrogen flow, followed by high vacuum for 8 h. Lipid mixtures were hydrated with 18 MΩ-cm water (EMD Millipore, Billerica, MA) at 47°C for 1 h, vortexing every 15 min. Samples were centrifuged at 14,000 × *g* for 30 min to form lipid pellets, and the supernatant removed. Pellets were transferred into *electron spin resonance* (ESR) capillary sample tubes and centrifuged again with a hematocrit centrifuge at 3300 × *g* for 30 min before the tubes were sealed. Samples were held at room temperature for a minimum of 5 h after centrifugation before recording spectra on an ELEXSYS E500 CW ESR Spectrometer (Bruker, Billerica, MA) operated at X-band frequency (9.4 GHz) with 0.5 Gauss modulation. Reported spectra are the average of 16 scans obtained at 20–24°C.

ESR spectra were modeled as a linear combination of Ld- and Lo-phase spectra with relative amounts corresponding to the relative fraction of 16PC in either phase (26–28). We analyzed the composite Ld + Lo spectrum for each ρ-value using the corresponding tieline endpoint Ld and Lo spectra, assuming the tieline endpoint Ld and Lo spectra changed linearly with ρ. In fact, the Ld and Lo spectra changed little over the entire range of ρ from 0 to 1. Fitting was performed by least squares minimization of the entire spectrum. Details of the fitting procedure are found in the Supporting Material. Using the fitted fractions of 16PC in the two phases, K_p values were determined by comparing the fraction of 16PC in either phase to the phase mole fraction obtained from the Lever-Arm Rule on the corresponding tielines (8). We use the convention that $K_p > 1$ corresponds to preference for Ld phase. For $\rho = 0$, 0.3, and 1, the tieline endpoint Ld and Lo ESR spectra were simulated (see Fig. S13) with nonlinear least squares analysis of slow-motional ESR spectra (26–28).

Determination of BODIPY-PC K_p *from fluorescence measurements*

BODIPY-PC K_p was measured in bSM/DOPC/POPC/chol spectrophotometrically in a cuvette, and in GUVs with a confocal fluorescence microscope, in both cases using a dye/lipid ratio of 1:2500. For single-dye fluorescence experiments, typically 61 samples were prepared along a

tieline. Phospholipid, chol, and dye were added in a glass tube using a repeating dispenser and a glass syringe. Aqueous buffer was added to each sample, and chloroform removed by rapid solvent exchange, as previously described in Buboltz and Feigenson (29), except that the equilibration started at 55°C, with cooling at 2°C/h to 23°C. Steady-state fluorescence was measured at ambient temperature (23°C) with excitation/emission wavelengths at 500/520 nm, slits 5/5 nm, and 10 s integration time using a model No. F-7000 FL Spectrofluorimeter (Hitachi High Technologies America, Schaumburg, IL). K_p values were determined as above (8). For microscopy experiments, GUVs of bSM/DOPC + POPC/Chol = 0.40/0.40/0.20 were formed by electroformation. Images were obtained at 23°C with a 60× water immersion objective. Additional details of K_p determination, including line scan protocols and self-quenching corrections, are described in the Supporting Material.

Model for calculating equilibrium domain size

Our approach to modeling domain size is to identify an interaction that could compete with line tension but not scale linearly with line tension. Dipole repulsion within the bilayer could be such an interaction, as described by Amazon and Feigenson (30). An initial question is whether dipoles in one leaflet would have their fields largely cancelled by the opposing dipoles in the other leaflet. This does occur for the terminal methyl dipoles that give rise to long-range repulsion in lipid monolayers (31), but the dipoles of interest in this study are located farther apart in the interfacial region.

To explore the implications of dipole repulsion for domain size, we modeled the total energy of a phase-separated bilayer as a sum of a phase boundary energy from line tension E_{perim} that scales with domain perimeter and an electrostatic potential energy E_{elec} arising from permanent lipid dipoles, with $E_{\text{total}} = E_{\text{perim}} + E_{\text{elec}}$. For N_D domains of total area α, $E_{\text{perim}} = 2\pi R_D N_D \sigma$, where σ is the line tension and $R_D = \sqrt{\alpha/(\pi N_D)}$ is the domain radius. For lipids distributed identically in the two bilayer leaflets and dipoles aligned with the bilayer normal, the total electrostatic potential energy of the bilayer is a sum of intra- and interleaflet contributions, i.e., $E_{\text{elec}} = 2V_{\text{intra}} + V_{\text{inter}}$, and

$$V_{\text{intra}} = N_D \frac{1}{2} \frac{N_L^2}{4\pi\varepsilon\varepsilon_0} \int_a^{2R_D} \frac{(\Delta\phi\varepsilon\varepsilon_0 A_L)^2}{r^3} P(r, R_D) dr, \quad (3)$$

$$V_{\text{inter}} = N_D \frac{N_L^2}{4\pi\varepsilon\varepsilon_0} \int_0^{2R_D} \left[\frac{3(h\Delta\phi\varepsilon\varepsilon_0 A_L)^2}{(h^2 + r^2)^{5/2}} - \frac{(\Delta\phi\varepsilon\varepsilon_0 A_L)^2}{(h^2 + r^2)^{3/2}} \right] P(r, R_D) dr, \quad (4)$$

where N_L is the total number of lipid dipoles per leaflet in the domain, A_L is the average lipid molecular area, h is the separation distance between opposing dipole layers, ε_0 is the permittivity of free space, ε is the dielectric constant (here, the dielectric constant of the bilayer region near the dipoles), $a = 2\sqrt{A_L/\pi}$ (the lower limit of the V_{intra} integral) is the distance of closest approach between two dipoles, and $\Delta\phi$ is the electrostatic potential difference between the domain and surrounding phase. The distribution of dipole separation distances $P(r,R_D)$ within the domain is given by the pair-distance distribution function for a disk (for details see the Supporting Material section Dipole-Dipole Repulsion Model),

$$P(r, R_D) = \frac{r}{\pi R_D^3} \left\{ 4R_D \tan^{-1}\left[\frac{R_D}{r} \sqrt{4 - (r/R_D)^2} \right] - r\sqrt{4 - (r/R_D)^2} \right\}. \quad (5)$$

This model does not explicitly treat the influence of the water and ionic strength. Instead, we made use of the finding by Zhou and Schulten (32) that the contribution of the lipid headgroups and the oriented water nearly cancel, so that the measured membrane dipole potential is determined by the lipid ester moieties. Additional details and a full derivation are found in the Supporting Material.

Nanodomain size measurements

Large unilamellar vesicle (LUV) samples for domain size measurements were prepared as follows. Lipid mixtures were prepared by transferring volumes of lipids and chol stocks in chloroform to a glass vial with a glass syringe (Hamilton USA, Reno, NV). Organic solvent was removed with a nitrogen stream and gentle heating, followed by vacuum drying for > 12 h. Dry lipid films were hydrated with a 34.5% (v/v) D_2O/H_2O mixture preheated to 50°C and vortexed to generate multilamellar vesicles (MLVs). The MLV suspension was incubated at 50°C for 1 h, followed by five freeze/thaw cycles between −80 and 50°C. LUVs were prepared using a Mini Extruder (Avanti Polar Lipids) assembled with a single polycarbonate filter (30-, 50-, 100-, or 200-nm diameter pore size) and heated to 50°C. Final sample concentrations were 10–20 mg/mL, which allowed for sufficient water between vesicles to eliminate the interparticle structure factor (33).

Small-angle neutron scattering (SANS) experiments were conducted at Oak Ridge National Laboratory (ORNL), using both the CG-3 BioSANS instrument of the High Flux Isotope Reactor and the BL-6 extended Q-range small-angle neutron scattering (EQ-SANS) instrument of the Spallation Neutron Source. LUV suspensions were loaded into 1 mm path-length quartz banjo cells (Hellma USA, Plainview, NY) and mounted in a temperature-controlled cell holder with ~1°C accuracy. BioSANS data were collected at a 14.5 m sample-to-detector distance using 6 Å wavelength neutrons (full width half-maximum 15%), resulting in a total scattering vector of $0.005 < q < 0.06$ Å^{-1}. EQ-SANS data were taken at a 4.0 m sample-to-detector distance with a 6.0–9.5 Å wavelength band for a total scattering vector of $0.01 < q < 0.1$ Å^{-1}. Scattered neutrons were collected with a two-dimensional (2D) (1 × 1 m) ^{3}He position-sensitive detector (ORDELA, Oak Ridge, TN) with 192 × 192 pixels (BioSANS) or 256 × 192 pixels (EQ-SANS). The 2D data were reduced using the software Mantid (34). During reduction, data were corrected for detector pixel sensitivity, dark current, and sample transmission, and the background scattering from water was subtracted. The one-dimensional scattering intensity $I(q)$ [$q = 4\pi \sin(\theta)/\lambda$, where λ is the neutron wavelength and 2θ is the scattering angle relative to the incident beam] was obtained by radial averaging of the corrected 2D data.

Nanodomain sizes were determined by analysis of $I(q)$ data using a coarse-grained Monte Carlo method described in Heberle et al. (11) and Pan et al. (35). Additional details are found in the Supporting Material.

MD simulations

Coarse-grained MD simulations were performed to characterize the size, shape, and dynamics of nanodomains. Simulations of phase-separated DPPC/DUPC/PUPC/chol systems with 20,000 total lipids were examined at ρ-values 0.5, 0.65, and 0.8. The simulations contained approximately four times as many lipids as previously studied for an identical composition (36), enabling consideration of the effect of system size on measured nanodomain properties. Bilayers were constructed using the CHARMM-GUI tool and then tiled to quadruple the system size (37–40). The Martini force field (version 2.1) was implemented in GROMACS 4.6.6 (41–44) using an NPT ensemble with a 30 fs time step under periodic boundary conditions in a box ~74 × 74 × 12 nm. A temperature of 295 K and pressure of 1 atm were maintained by a V-rescale thermostat (time constant 1 ps) and semiisotropic Parrinello-Rahman barostat (time constant 12 ps), respectively. Temperature bath coupling was separate for lipids and solvent. The GPU-compatible Verlet cutoff scheme was used with electrostatic and van der

Waals potentials shifted to reach zero at 1.1 nm. Center-of-mass motion was removed each 10 time steps. All simulations were conducted on Titan at the Oak Ridge Leadership Computing Facility.

Analysis was performed using a custom Python script incorporating the MDTraj library (45). A Voronoi tessellation of lipids in a single leaflet determined each molecule's nearest neighbors as those with which it shared a Voronoi ridge. Phase determination for each lipid was based on the lipid and its nearest neighbors, with enrichment in DPPC and chol serving as a marker of the Lo phase, and depletion of these lipids a marker of the Ld phase. For details, see the Supporting Material.

RESULTS

The mixtures examined here are described by phase diagrams of the type shown in Fig. 1 A for a three-component lipid mixture of DSPC/DOPC/chol (9). More generally, this phase behavior occurs for mixtures of the type (high-T_m PC or sphingomyelin)/(low-T_m PC)/chol, as found by several researchers (46,47). Important for our studies is that a mixture is separated into immiscible liquid domains. To study this behavior, we employ vesicles of different size and lamellarity (LUVs, GUVs, and MLVs) as dictated by the constraints of different experimental techniques. Whereas vesicle size constrains the maximum possible domain size, curvature has no measurable effect on the structure of PC bilayers for vesicle diameters larger than 50 nm (33,48) as used in this study. Furthermore, although the presence of multiple lamellae increases the cooperativity of phase transitions in single component bilayers, the same transitions are nevertheless seen in LUVs, GUVs, and MLVs (49). These findings suggest that vesicle size and curvature do not significantly affect phase behavior.

Phase boundaries, as shown in Fig. 1 A, have been determined as described in the literature (7–9,22), mainly using steady-state fluorescence spectroscopy, fluorescence microscopy, ESR, and differential scanning calorimetry. Other researchers have found similar boundaries by use of nuclear magnetic resonance and x-ray diffraction (46,50,51). The mixture DSPC/POPC/chol is described by a similar phase diagram to that in Fig. 1 A (9), except that the coexistence of Ld + Lo domains was detected by Förster resonance energy transfer, ESR, and SANS, but not visualized with optical microscopy, suggesting domains of a size below the optical resolution limit (11,12). In the four-component lipid mixture DSPC/DOPC/POPC/chol, this transition can be explored with the replacement of POPC by DOPC, where ρ = [DOPC]/[DOPC + POPC], as in Fig. 1 B. As described below, we measured how physical properties, including domain size, line tension, bending rigidity, order and rotational diffusion of a probe, and probe partitioning, change along this ρ-trajectory.

Domain size exhibits an abrupt transition with composition that is correlated with line tension

We recorded the visual appearance of domains examined in GUVs with fluorescence microscopy. Fig. 1 C shows images of GUVs composed of DSPC/DOPC/POPC/chol having compositions along a ρ-trajectory and is a representative example for all mixtures studied. For $\rho = 0$ and 0.1, GUVs appeared uniform, but Förster resonance energy transfer, ESR, and SANS studies revealed nanodomains with sizes below optical resolution (8,9,22). At higher ρ-values from 0.4 to 1, GUVs exhibited large, round domains with micron-sized diameters. In the course of the transition between GUVs with uniform appearance and GUVs with large and round domains, we observed a composition range where GUVs showed modulated phase patterns; we previously termed this region the "ρ-window" (9,10,13,16). Fig. 1 C reveals modulated phases for DSPC/DOPC/POPC/chol at $\rho = 0.2$ and 0.3. These modulated phase patterns mark the first appearance of visible domains, and thus a pronounced change in domain size from tens of nanometers to microns.

Similar abrupt domain size transitions were observed for 12 other mixtures, although at different ρ-values for each mixture, as shown in Fig. 2. The fraction of GUVs exhibiting either modulated phases or round macroscopic domains is indicated by a solid line in Fig. 2; we emphasize this sum because it better represents the domain size transition from nanodomains (uniform GUVs) to visible domains. For convenience in the following discussion, we define ρ^* as the composition at which half of GUVs have visible domains. Below, we show that ρ^* is correlated with line tension. As shown in Fig. 2, the size transition marked by ρ^* depended upon both the high-T_m and the low-T_m lipids. For example, in mixtures of DOPC/POPC/chol with the high-T_m lipids pSM, eSM, DSPC, or bSM, ρ^* appeared at 0, 0.07, 0.24, and 0.52, respectively (Fig. 2, A, C, F, and I). The nature of the low-T_m nanodomain-forming PC also affected ρ^*: For mixtures of bSM/DOPC/chol with the components 16:0,18:2-PC, POPC (16:0–18:1PC), or SOPC (18:0–18:1), ρ^* appeared at 0.45, 0.52, and 0.58, respectively (Fig. 2, H, I, and J). Thus, increased unsaturation and shorter acyl chains of the low-T_m nanodomain-forming lipid shifted ρ^* to lower values in these mixtures, consistent with a previous report that a thinner Ld phase results in a greater hydrophobic mismatch and possibly a higher line tension (11) inducing the formation of visible domains at lower ρ. Also consistent with thickness mismatch-driven line tension is the observation that low-T_m macrodomain-forming PCs with different hydrophobic thickness resulted in different ρ^* values: in mixtures with DSPC/DLPC/chol (Fig. 2, D and G) and DSPC/POPC/chol (Fig. 2, E and F), a smaller amount of DPhPC (hydrophobic thickness 27.2 Å at 30°C (48)) compared to DOPC (hydrophobic thickness 29.1 Å at 30°C (52)) was needed to form macroscopic domains. Finally, contrary to theoretical predictions that hybrid and nonhybrid lipids should behave differently (53), DLPC and POPC resulted in a nearly identical ρ-window (13,54) in mixtures with DSPC/DOPC/chol (Fig. 2, F and G).

We also examined mixtures with compositions that are closer to that of the PM. In bSM/SDPC/POPC/chol (55),

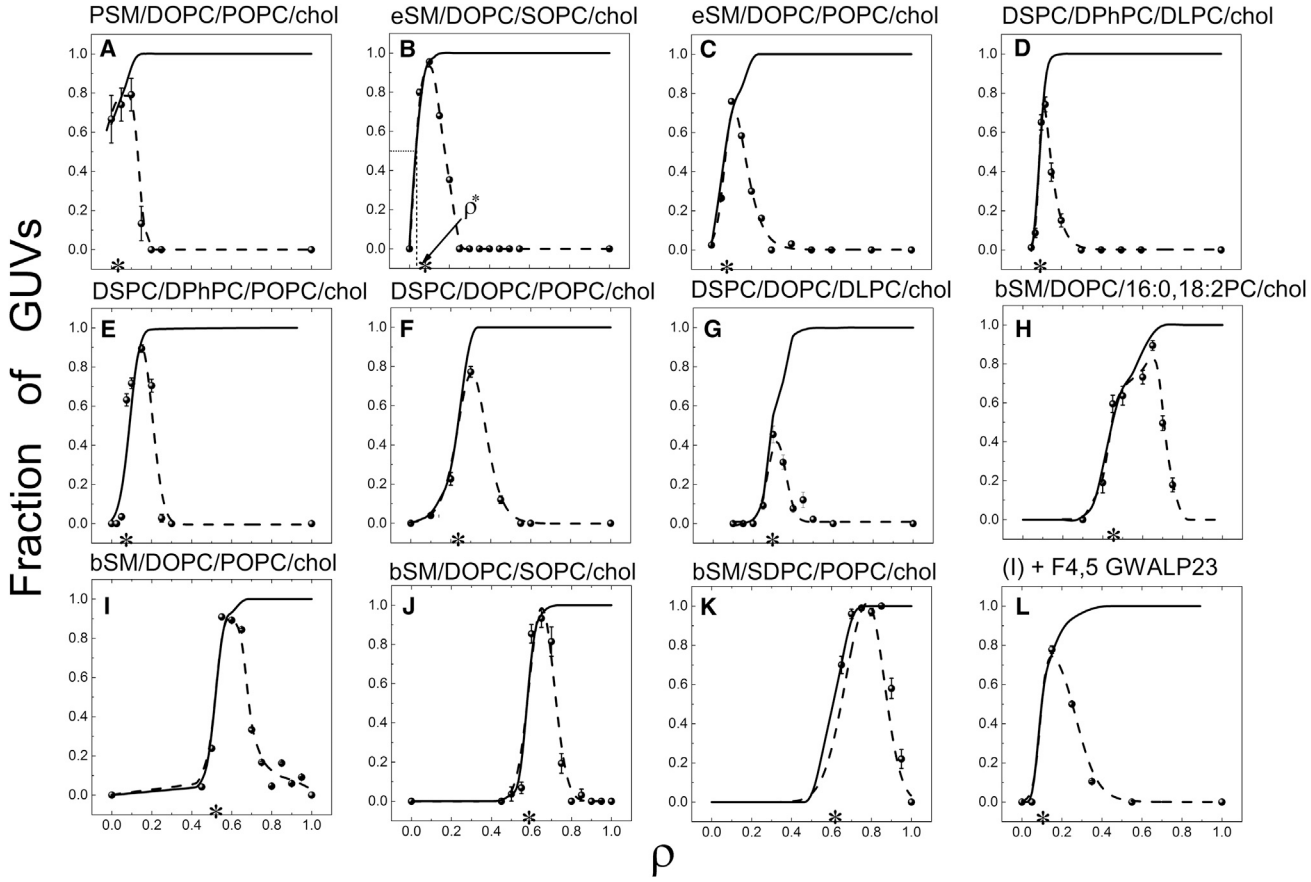

FIGURE 2 (*A–L*) Morphology of coexisting Ld + Lo domains changes with ρ. In GUVs prepared from four-component lipid mixtures, phase domain morphology changes from uniform (i.e., no visible domains), to modulated patterns, to macroscopic round domains as ρ is varied from 0 to 1. The fraction of GUVs showing modulated domain morphology is plotted as a function of ρ for different four-component lipid mixtures (*dashed lines*). (*Solid line*) Fraction of GUVs showing modulated phases + the fraction of GUVs showing macroscopic domains. (*Asterisk*) Midpoint of the domain size transition, denoted as ρ^*. Data for (*F*), (*G*), and (*K*) originally appeared in Heberle et al. (54), Goh et al. (13), and Konyakhina and Feigenson (55), respectively. Lipid compositions of GUVs are described in Table S1.

we found a high ρ^* value of 0.61 (Fig. 2 K), an indication of enhanced stability of nanoscopic domains. In contrast, a mixture containing an α-helical transmembrane peptide appears to have a markedly increased line tension. Fig. 2, I and L, shows the ρ-trajectory for bSM/DOPC/POPC/chol in the absence and presence of 4 mol % of $F^{4,5}$GWALP23, respectively, revealing a decrease in ρ^* from 0.52 to 0.1 induced by the peptide.

We used GUV flicker spectroscopy to measure line tension for six mixtures, shown in Fig. 3. Comparing these data to the ρ-windows in Fig. 2, several trends are apparent: 1) for each of the mixtures, the ρ-value where micron-scale domains first appeared corresponds to a line tension of ~0.3 pN; 2) large, round domains always correspond to line tensions >~1.1 pN; 3) line tension values for high-T_m sphingomyelins followed the trend pSM > eSM > bSM in mixtures with DOPC/POPC/chol, consistent with a progressively higher ρ-window for SM in this series, with $\rho^* = 0.1$, 0.15, and 0.55, respectively (Fig. 2, A, C, and I); 4) with the high-T_m lipid DSPC, similar line tensions and ρ^* values were found in mixtures with DPhPC/DLPC/chol and with DPhPC/POPC/chol, whereas lower line tension and a higher ρ^* were found with DOPC/POPC/chol. We conclude that changes in ρ^* for these lipid mixtures reflect changes in the Ld/Lo line tension.

Physical and chemical properties of Ld and Lo phases do not change at the abrupt domain size transition

We measured a phase property of the bilayer, the bending modulus κ, for single-phase GUVs. These measurements were performed separately for Ld and Lo compositions from the nanoscopic to the macroscopic regime ($\rho = 0$–1), including the region where an abrupt domain size transition occurs. Fig. 4 shows the bending moduli of the Ld and Lo phases, κ_{Ld} and κ_{Lo}, for DSPC/DOPC/POPC/chol. As ρ was varied from 0 to 1, κ_{Ld} decreased from 1.9 to 1.1 $\times$ 10^{-19} J, while κ_{Lo} increased from 7.3 to 10.4 $\times$ 10^{-19} J. For both the Ld and Lo phases, variation in bending moduli over the entire

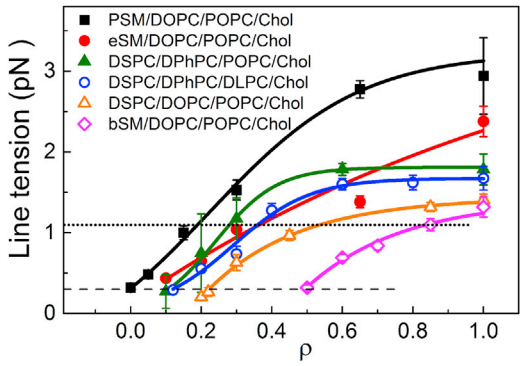

FIGURE 3 Line tension increases in a ρ-trajectory. Line tension for six four-component lipid mixtures measured with GUV flicker spectroscopy. In all mixtures, visible domains first appear at ~0.3 pN (*dashed line*), while domains become fully rounded at ~1.1 pN (*dotted line*). Line tension was measured by fluctuation analysis of either an Lo or Ld domain using wide-field fluorescence microscopy at 23°C with fluorescent dye C12:0-DiI at 0.2 mol %. Error bars correspond to SE.

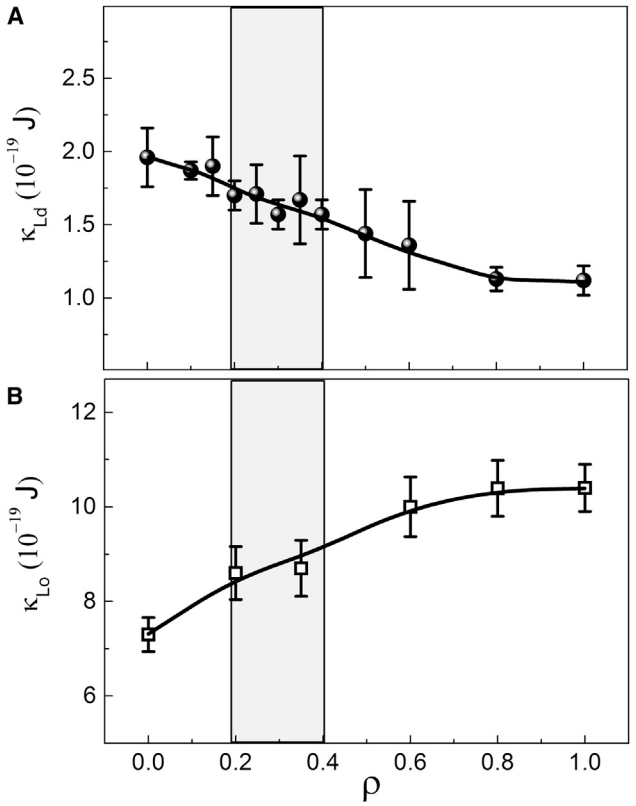

FIGURE 4 Lo and Ld bending moduli do not show abrupt transitions in a ρ-trajectory. The bending modulus of (*A*) Ld phase (κ_{Ld}) and (*B*) Lo phase (κ_{Lo}) measured at different ρ-values in DSPC/DOPC/POPC/chol. As POPC is replaced by DOPC (i.e., increasing ρ), κ_{Ld} gradually decreases, while κ_{Lo} gradually increases. Within the ρ-window where domain size exhibits an abrupt increase (*shaded region*), changes in bending rigidity of either phase are <10%. Error bars correspond to SE ($n > 5$).

ρ trajectory was less than twofold, and only 5–10% within the region of abrupt domain size change indicated by the shaded regions (corresponding to the ρ-window of Fig. 2 F).

We also measured the partition coefficient K_p between Ld + Lo domains of a fluorescent probe, BODIPY-PC, and an ESR probe, 16PC, in the composition range $\rho = 0$–1. Here, $K_p = [\text{probe}]^{Ld}/[\text{probe}]^{Lo}$ and $K_p > 1$ indicates preference for Ld phase. Fig. 5 *A* shows the K_p of BODIPY-PC in bSM/DOPC/POPC/chol obtained either from fluorescence microscopy measurements of GUVs (*open triangles*) or from fluorescence spectroscopic measurements (*solid circles*), revealing good agreement between these methods. The K_p of BODIPY-PC increases from 3 to 9 over the composition range $\rho = 0$–1, and by ~30% in the vicinity of the abrupt domain size transition indicated by the shaded region (corresponding to the ρ-window of Fig. 2 I). For the ESR probe 16PC, K_p values in DSPC/DOPC/POPC/chol increase from 0.7 to 1.8 over the composition range $\rho = 0$–1 (Fig. 5 B). There are no abrupt changes in K_p, and in particular <10% change in the shaded region corresponding to the ρ-window of Fig. 2 F, where domain size changes hundreds of fold. Moreover, the order parameter S_0 and rotational diffusion coefficient $R_\perp$ of 16PC in the Ld and Lo phases hardly changed: Table 1 shows nearly constant values of S_0 and $R_\perp$ for $\rho = 0$, 0.3, and 1, representative of nanoscopic, transition, and macroscopic compositions. We conclude that physical and chemical properties of Ld and Lo phases do not undergo abrupt changes despite the abrupt change in domain size that occurs along a ρ-trajectory.

Competing interactions could drive the domain size transition

With no evidence of an abrupt transition in several properties characteristic of Ld and Lo phases, we next explored what kind of interaction could lead to an abrupt transition in domain size. We modeled the dependence of domain size on line tension together with dipole-dipole repulsion that could originate, for example, in the permanent dipoles of the carbonyl-glycerol backbone (Fig. S14). Fig. 6 A shows the energies of the individual competing interactions (i.e., boundary energy arising from line tension and electrostatic energy arising from dipole-dipole repulsion) as a function of domain radius, calculated for a line tension of 0.25 pN. Fig. 6 B reveals that the total energy is minimized at a particular domain size, which we define as the equilibrium domain radius R_d*. Fig. 6 C shows R_d* as a function of line tension. At very low line tensions, electrostatic repulsion dominates and numerous small domains are favored. At high line tensions, the boundary energy dominates and a single, large domain is favored. These two competing interactions are balanced at intermediate line tensions, resulting in stable domains with nanoscopic sizes. The precise location of the transition is influenced by the choice of model parameters: for example, increasing the Ld/Lo electrostatic potential difference $\Delta\phi$ from 0.1 V (*solid line*) to 0.2 V (*dot-dashed line*) increases domain repulsion, thereby stabilizing nanodomains to higher line tension values.

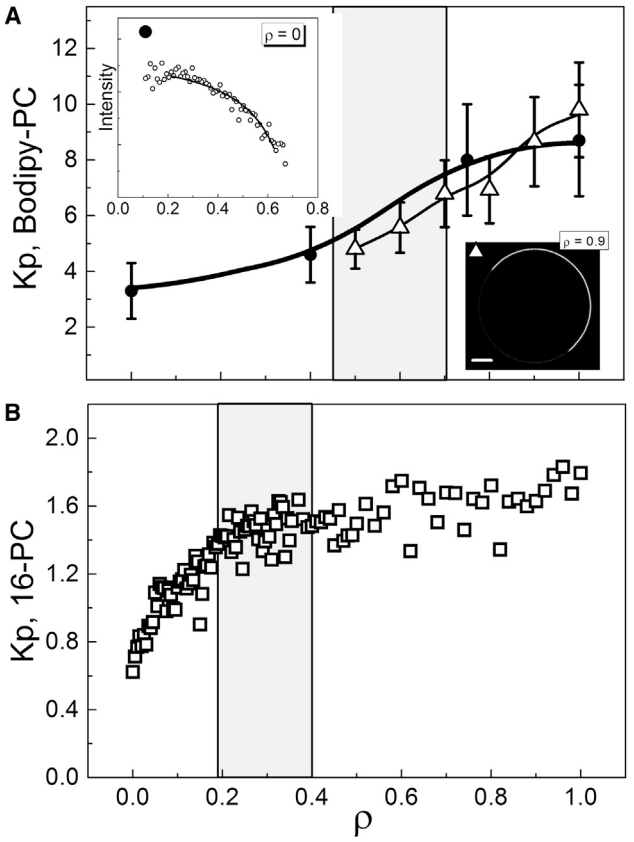

FIGURE 5 Probe partition coefficients do not show abrupt transitions along a ρ-trajectory. Partition coefficient K_p between Ld and Lo phases for: (*A*) the fluorescence probe BODIPY-PC in bSM/DOPC/POPC/chol, and (*B*) the spin-label probe 16PC in DSPC/DOPC/POPC/chol. Within the ρ-window where domain size exhibits an abrupt increase (*shaded regions*), changes in K_p are gradual. Also shown in (*A*) are: (*upper-left inset*) the fluorescence intensity (*symbols*) and fit to a partitioning model (*solid line*) of Bodipy-PC along a thermodynamic tieline at $\rho = 0$, and (*lower-right inset*) fluorescence micrograph revealing the partitioning of Bodipy-PC in a GUV at $\rho = 0.9$ (scale bars, 5 μm, temperature 23°C). For details, see the Supporting Material.

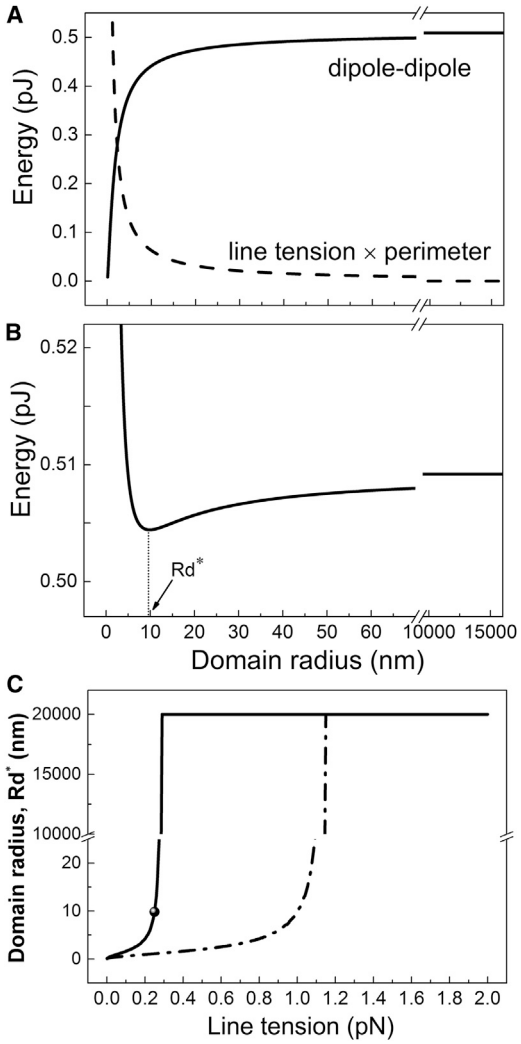

FIGURE 6 A model of competing interactions describes the domain size transition. (*A*) Energetic contributions from domain interface (line tension × perimeter) and dipole-dipole repulsion as a function of domain radius, calculated for a line tension value of 0.25 pN. (*B*) The sum of interfacial and electrostatic energy in (*A*) exhibits a minimum value at domain radius R_d*. (*C*) R_d* plotted versus line tension reveals an abrupt domain size transition for model parameters $\varepsilon = 8$, $h = 3.0$ nm, $A_L = 60$ Å^2, and $\Delta\phi = 0.1$ V (*solid line*) or 0.2 V (*dot-dashed line*). A description of model parameters is found in the Supporting Material.

We further examined several model parameters to find the line tension value where the domain size transition occurs (Figs. S15 *B* and S16). The critical line tension value λ* at which domain size abruptly increases depends strongly on the dipole potential difference: we found that varying $\Delta\phi$ over the range 0.05–0.5 V resulted in λ* values increasing from 0.08 to 8 pN. Large changes were also observed upon varying the dielectric constant ε over the range 2–20, which resulted in λ* increasing from 0.05 to 0.8 pN. In contrast, varying the separation distance of the dipole layers h, or the area per dipole A_L, had negligible influence on the critical line tension value. Although the precise line tension value at the domain size transition depends on the choice of model parameters, the finding of an abrupt transition is robust. It occurs for a wide range of parameter values, as well as in related models where the domain potential is treated as arising from discrete dipoles, or from pairs of discrete charges, or where the electrostatics of both the domain and the surrounding in a spherical phase-separated

TABLE 1 ESR Reveals Small Changes of Ld and Lo Phases along the Domain Size Transition

	Ld Phase		Lo Phase	
ρ	S_0	$R_\perp$ ($\log_{10}$ s^{-1})	S_0	$R_\perp$ ($\log_{10}$ s^{-1})
0	0.13	8.4	0.36	8.6
0.3	0.12	8.5	0.36	8.6
1.0	0.11	8.5	0.34	8.5

Order parameter, S_0, and rotational diffusion coefficient, $R_\perp$, of the spin probe 16PC in Ld and Lo phases for different ρ-values that represent nanoscopic, transition, and macroscopic lipid compositions.

vesicle are treated separately. These results are presented in the Supporting Material.

Nanoscopic domains are not significantly influenced by vesicle size, but have a complex shape

In the nanoscopic regime, GUVs appear uniform (e.g., Fig. 1 C, $\rho = 0$ and 0.1), thus different experimental methods are required to study the coexistence of Ld + Lo domains. We used SANS to measure domain size in 50- and 100-nm diameter LUVs composed of DSPC/DOPC/POPC/chol, finding only a small influence of vesicle size on nanodomain size as a function of ρ (Fig. 7). Additional details about the minimal dependence of nanodomain size on LUV size are found in the Supporting Material.

Our SANS model assumes round nanodomains to facilitate analysis. However, coarse-grained MD simulations revealed a more complex domain morphology. Fig. 8 shows a characteristic simulation snapshot of a nanodomain for $\rho = 0.65$ after 3.6 μs of simulation, together with a circular outline diameter of ~25 nm as a reference. These simulations show that nanodomains are in general not circular. Rather, they display complex and dynamic morphology, even in an equilibrated system long after separation into coexisting Ld + Lo domains.

DISCUSSION

As we show in this work, the energy per unit length of the interface (i.e., the line tension) in a phase-separated bilayer can be dramatically influenced by lipid composition, thereby driving changes in interface length and thus domain size. Cells could control the size of coexisting domains in the PM and thereby modulate signaling simply by changing the high-T_m or the low-T_m lipids, or any other factors that change line tension. We used four-component mixtures to control the transition of coexisting Ld + Lo domains from nanoscopic to macroscopic sizes (10). The high-T_m lipids we examined were pSM, bSM, eSM, and DSPC, chosen for biological prevalence or because of extensive prior characterization. The low-T_m lipids were POPC, DOPC, DLPC, SDPC, and DPhPC, chosen either for biological prevalence or because these lipids create macroscopic Ld + Lo domains.

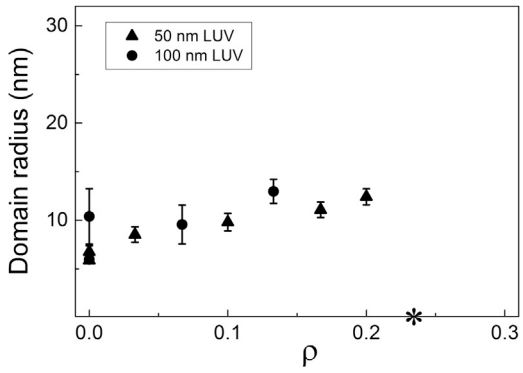

FIGURE 7 SANS reveals domain size in the nanoscopic regime along ρ. Domain radius obtained from Monte Carlo modeling of SANS data for LUVs composed of DSPC/DOPC/POPC/chol. Within the nanoscopic regime at $\rho < 0.2$, domain radius increases gradually from 6 to 12 nm for LUVs of either 50 nm diameter (*triangles*) or 100 nm diameter (*circles*). The asterisk marks ρ*, where 50% of the GUVs were observed with modulated phases or with macrodomains.

FIGURE 8 Simulated nanodomains have a complex morphology. A top-down view of a nanodomain in a coarse-grained MD simulation of DPPC/DUPC/PUPC/chol at $\rho = 0.65$ reveals a complex, noncircular domain shape. Voronoi cells of lipids in the Lo phase are shown in black, while those in the Ld phase are shown in white. The snapshot was obtained after 3.6 μs of simulation at a temperature of 22°C. A dashed gray circle of 25 nm diameter is shown as a reference.

The domain size transition is correlated with line tension

As ρ is increased, Ld and Lo domains in each of the mixtures in Fig. 2 undergo a change in size of two orders of magnitude at ρ*, from tens of nanometers in diameter to the visible micron scale. This size increase occurs over a change of only ~2–5% in the total lipid composition, which corresponds to ~20% variation in ρ. This width of the ρ-window also has a component from the compositional variation of individual GUVs that has been estimated to be ± 5 mol % (56), so the true size change could be even more abrupt.

For the mixtures shown in Fig. 3, the line tension value where macroscopic domains first appear is in every case ~0.3 pN. It is possible that an interaction that competes with line tension, e.g., dipole-dipole repulsion, is overwhelmed by a line tension of 0.3 pN. The domain size

just below this ρ-value might provide information on the dipole magnitude and dielectric constant in that region of the bilayer. Another possibility is that below 0.3 pN, thermal fluctuations break up domains.

Comparing Figs. 2 and 3, ρ^* occurs at a line tension of ~1.1 pN for each mixture. We previously modeled the domain size transition as arising from a competition between line tension and curvature (16) and found that this model could reproduce experimental observations including modulated phase patterns (10,13). Bending energy opposes line tension by penalizing large domains of the stiffer Lo phase on curved surfaces, and macroscopic patterns occur when the two interactions are more balanced. Modulated morphology might give way to rounded macroscopic domains at roughly the same value of line tension perhaps because the rigidity difference between Ld and Lo is similar for the mixtures studied here.

Another simple relationship emerges from a comparison of Figs. 2 and 3, namely that smaller values of ρ^* in every case correspond to higher values of the line tension. A higher ρ^* can therefore be a useful surrogate for lower line tension: compared to the conditions needed to determine line tension, a 10-fold lower dye concentration and ~10-fold lower cumulative light exposure are needed to determine ρ^*, resulting in a much lower probability of photochemical artifacts (21). Using ρ^* data we can therefore more readily investigate mixtures containing unstable polyunsaturated lipids. For example, photochemical instability of the 22:6 acyl chain of SDPC precludes measuring line tension, yet phase boundaries (55) as well as ρ^* could be determined for the mixture, bSM/SDPC/POPC/chol (Fig. 2 K). The strikingly high value of $\rho^* = 0.61$ indicates quite low line tension until the mixture has a high fraction of SDPC. In a sense, line tension is just barely enough for bSM/SDPC/chol phase domains to be macroscopic. Another interesting case is bSM/DOPC/POPC/chol with a significant fraction of transmembrane helical peptide as a component. Upon adding the α-helical peptide GWALP23 to the otherwise lipid-only mixtures, ρ^* drops from $\rho = 0.52$ to 0.1 for bSM/DOPC/POPC/chol (Fig. 2, I and L), and from $\rho = 0.58$ to 0.3 for bSM/DOPC/SOPC/chol (S.P.W., unpublished data). These observations reveal that this peptide significantly increases the line tension. In a previous MD simulation we found that GWALP23 is depleted from the Ld/Lo interface, consistent with the peptide increasing line tension (57).

Properties of Ld and Lo domains do not change abruptly despite the abrupt domain size transition

We studied different properties of Ld and Lo phases along the domain size transition from nanoscopic to macroscopic phase separation. Well-resolved phase diagrams were required for this work. A previously determined four-component phase diagram enabled finding phase boundaries for each ρ-value in the representative mixture DSPC/DOPC/POPC/chol (9). Although our compositional trajectories were always within the Ld + Lo coexistence region, the tieline endpoints change with ρ. Accurate phase boundaries are needed to apply the Lever-Arm Rule to study Lo and Ld properties such as bending modulus, order parameter, rotational diffusion, and probe partition between these phases. Defining ρ^* for each mixture enabled our finding that the abrupt increase in domain size is not accompanied by abrupt changes in any measured Ld and Lo phase properties. A potentially important corollary is that because no abrupt changes with domain size are observed in the particular properties we chose to measure here, we suggest that measurement of these properties in the macroscopic regime is likely to reflect the properties of the nanoscopic domains. In general, it is more convenient to measure macroscopic domain properties, which we here establish as providing useful information about nanoscopic domain properties.

We measured the bending modulus for both Ld and Lo phases over the entire range of ρ-values. In the compositional range where domain size changes dramatically (the *shaded regions* in Fig. 4), the bending moduli change by just a few percent. The Ld bending modulus decreases with increasing ρ (i.e., increasing DOPC; Fig. 4 A), consistent with observations that single-component membranes of low-T_m lipids with one saturated chain, like POPC, are rigidified by cholesterol while DOPC membranes are not (24,25,58,59). The DSPC/DOPC/POPC/chol phase diagram (9) indicates that the Ld composition does not depend on ρ, having a similar concentration of DSPC, low-T_m lipid, and chol at all ρ-values. In contrast, the Lo composition contains proportionally more DSPC and chol, and less low-T_m lipid, as ρ increases. Consequently, the Lo phase bending modulus increases with increasing ρ (Fig. 4 B).

Another phase-dependent property characteristic of coexisting Ld + Lo domains is the partition coefficient K_p for a molecule that can equilibrate between the two environments. We measured K_p for the mixtures DSPC/DOPC/POPC/chol (Fig. 5 B) and bSM/DOPC/POPC/chol (Fig. 5 A). For both a paramagnetic ESR probe (16PC) and a fluorescent probe (BODIPY-PC), we observed compositional dependence as ρ was varied from 0 to 1, with K_p increasing by approximately threefold over the entire range of ρ, but without abrupt changes at the composition ρ^* where domain size changes abruptly in both lipid mixtures. Another finding emerges from the single dye fluorescence experiments performed in the nanoscopic regime: simple, hyperbolic partitioning curves are observed in both the nanodomain region (Fig. 5 A, *left inset*) and the macrodomain region (raw data not shown). We conclude that Ld and Lo phase fractions in the nanoscopic regime follow the Lever-Arm Rule just like macroscopic phase separation.

Using ESR, we also examined the order parameter and rotational diffusion rate of 16PC in Ld and Lo phases of DSPC/DOPC/POPC/chol. Changes in these parameters

were surprisingly small (Table 1), consistent with only gradual variation in phase properties.

Competition between line tension and dipole repulsion drives the domain size transition

What is responsible for the abrupt increase in domain size observed for 12 different mixtures? A simple model of line tension competing with dipole repulsion reproduces the abrupt domain size transition observed in experiments (Fig. 6). The model relies on the dipoles in each leaflet being far enough apart as not to cancel, having a significant component oriented along the bilayer normal, and being located in a low enough dielectric that the field persists for several lipid neighbors. We do not know the dielectric constant in part because we do not know the actual dipole location. We also do not know the difference in dipole density between Lo and Ld domains, because that would require measurements of the Lo phase that are not yet reliable. Still, reasonable ranges of these parameters all show an abrupt domain size transition (Figs. S15 and S16).

We do not know which dipoles might be involved in limiting domain size. We chose to model repulsion that would be consistent with carbonyl groups, in part because experiments with ether-linked chains show a decrease in bilayer potential (60), although such experiments do not rule out the very real possibility that ester- versus ether-induced conformational changes could influence a measured dipole potential. Also, the carbonyl-carbonyl distances across the bilayer are relatively well defined and thus suitable to model. An oriented bound water molecule could be a source of dipole-dipole repulsion, if located in a low dielectric region such that the electric field would persist over several lipid neighbors. In these symmetric bilayers, dipoles of the terminal methyls could not be the source of the repulsion as they are in lipid monolayers, because the apposing leaflet methyl dipoles would be so close and of the same type of phase (and thus the same motional and orientational state) as to cancel. However, we do not rule out that in asymmetric bilayers the terminal methyls could contribute to dipole-dipole repulsion. Additionally, the methyl dipoles might contribute significant electrostatic repulsion for nanodomains that are not in register across the leaflets (61). In brief, we have not proven that our treatment of dipole-dipole repulsion correctly describes the interaction that occurs on the tens of nanometer scale to compete with line tension. We have only shown that with reasonable values of key parameters, the difference of dipole potential between Ld and Lo domains and the dielectric constant near those dipoles, the observed behavior is reproduced in our model: domain size abruptly changes by two orders of magnitude with a small change in line tension.

It could be that for line tension $<$~0.3 pN the amplitudes of thermal fluctuations are sufficient for preventing the coalescence of domains. This could occur, for example, if the fluctuations approached the size of the domains themselves. For example, at $\rho = 0$, domain diameter measured by SANS is ~15 nm (Fig. 7). Fluctuations of this magnitude would occur with a line tension of ~0.1 pN (23). However, this consideration does not address the dramatic size change observed experimentally. In this regard, MD simulations have shown that registration of domains together with domain size both dramatically increase at a domain size of ~15 nm (36). These findings point to enhanced coupling of the two leaflets and domain stability both being enabled at a particular domain size. Because these are observations from MD simulations, which would include implicitly any dipole-dipole effects, we are not able to separate these effects in the simulations.

Hybrid and nonhybrid lipids have similar line activity

We have previously concluded that emphasis on a special behavior of hybrid lipids in forming nanodomains is misleading (54). For five of the six mixtures shown in Fig. 3, we used POPC as the nanodomain-forming low-T_m lipid. Starting at $\rho = 1$ where line tension is greatest, the ρ-trajectory could be described as substituting a fraction of POPC into the high line tension mixture. In four of the mixtures, POPC hardly lowers line tension until it becomes nearly 40 mol % of the low-melting lipid. When the nanodomain-forming low-T_m lipid is DLPC instead of POPC, the same result is observed. These experiments suggest that hybrid lipid POPC behaves similarly to the nonhybrid lipid DLPC to decrease line tension. Both POPC and DLPC might be described as weakly line active.

Nanodomains have a complex morphology

The large MD simulations performed in this study better reveal nanodomain size and morphology. Compared to previous studies (36), our large box size of 74 $\times$ 74 nm allowed for multiple independent Lo nanodomains to exist in the Ld surround in a leaflet of coexisting Ld + Lo phases. We find nanodomain size to be consistent with SANS measurements, on the order of 25 nm. In a 3.6 μs simulation at $\rho = 0.65$ (see the Supporting Material for a movie and simulation snapshots at other ρ-values), after the first microsecond of equilibration, nanodomains are easily recognized, but their morphology is highly dynamic throughout the simulation, and it is never circular.

CONCLUSIONS

We investigated the nature of the abrupt domain size transition observed in four-component lipid mixtures mimicking the PM composition. We find that various Ld and Lo phase properties measured as functions of ρ can be explained by treating Ld + Lo nanodomains as coexisting phase domains, and that the domain size transition does not appear to be a

phase transition. However, the more important point is the phenomenon itself, namely that coexisting nanoscopic domains containing hundreds to thousands of lipids coalesce over a narrow composition range into domains hundreds of times larger. We find that line tension is the key parameter that controls this size transition, and line tension depends strongly on the nature of both the high-T_m and low-T_m lipids. In summary:

1) The size of coexisting Ld + Lo domains changes abruptly in composition space.
2) Line tension has the decisive role in controlling the abrupt size transition.
3) Ld or Lo phase parameters show only gradual changes even as domain size changes abruptly.
4) Phase behaviors measured for Ld + Lo macrodomains are a good surrogate for behaviors of nanodomains.
5) Hybrid lipids 18:0,22:6-PC, 16:0,18:1-PC, 16:0,18:2-PC, or 18:0,18:1-PC reduce line tension only weakly.
6) Visible Ld + Lo phase domains first appear at line tension ~0.3 pN in six different lipid mixtures.
7) Dipole repulsion within the bilayer might stabilize nanodomains.
8) MD simulations of a large patch of lipids show that a nanodomain is not round, but has complex and fluctuating morphology.

SUPPORTING MATERIAL

Supporting Materials and Methods, sixteen figures, four tables, and one movie are available at http://www.biophysj.org/biophysj/supplemental/S0006-3495(17)30248-5.

AUTHOR CONTRIBUTIONS

R.D.U. and T.A.E. designed and performed the research, analyzed the data, cowrote the article, and contributed equally to the work; S.P.W., M.D.W., W.-C.T., M.B.K., and S.W. designed and performed the research and analyzed the data; T.L.T. and J.K. designed experiments; D.G.A. and F.A.H. designed and performed the research, analyzed the data, and cowrote the article; and G.W.F. designed the research, analyzed the data, and cowrote the article.

ACKNOWLEDGMENTS

We thank Peter Olmsted and Kevin Brown for helpful comments, and Roger Koeppe and Denise Greathouse for kindly providing the peptide GWALP23.

This work was supported by U.S. National Science Foundation grant No. MCB-1410926, U.S. National Institutes of Health grant No. GM105684, and OLCF/Titan grant No. DD-2015-BIP125 (to G.W.F.); NIH Training grant No. 1-T32-GM08267 (to D.G.A. and M.D.W.); National Science Foundation Graduate Research Fellowship Program under grant No. DGE-1144153ESR (to R.D.U.); Brazil Conselho Nacional de Desenvolvimento Científico e Tecnológico, CNPq (to T.A.E.); the University of Tennessee-ORNL Joint Institute for Biological Sciences (to F.A.H.); and the Laboratory Directed Research and Development Program (to J.K. and F.A.H.) of ORNL, managed by UT-Battelle under US Department of Energy (DOE) contract No. DE-AC05-00OR22725. ESR studies were supported by NIH/NIGMS grant No. P41GM103521 to J. Freed. Neutron scattering studies conducted using the EQ-SANS instrument at the ORNL Spallation Neutron Source, and the BioSANS instrument at ORNL's High Flux Isotope Reactor, were sponsored by the Scientific User Facilities Division of the DOE Office of Science, Basic Energy Sciences (BES) and Biological and Environmental Research (BER). The MD simulations in this work used resources of the Oak Ridge Leadership Computing Facility at the ORNL, which is supported by the Office of Science of the U.S. Department of Energy under contract No. DE-AC05-00OR22725.

REFERENCES

1. Quehenberger, O., A. M. Armando, …, E. A. Dennis. 2010. Lipidomics reveals a remarkable diversity of lipids in human plasma. *J. Lipid Res.* 51:3299–3305.
2. Sampaio, J. L., M. J. Gerl, …, A. Shevchenko. 2011. Membrane lipidome of an epithelial cell line. *Proc. Natl. Acad. Sci. USA.* 108:1903–1907.
3. Takamori, S., M. Holt, …, R. Jahn. 2006. Molecular anatomy of a trafficking organelle. *Cell.* 127:831–846.
4. Lomize, M. A., A. L. Lomize, …, H. I. Mosberg. 2006. OPM: orientations of proteins in membranes database. *Bioinformatics.* 22:623–625.
5. Lin, Q., and E. London. 2015. Ordered raft domains induced by outer leaflet sphingomyelin in cholesterol-rich asymmetric vesicles. *Biophys. J.* 108:2212–2222.
6. Feigenson, G. W., and J. T. Buboltz. 2001. Ternary phase diagram of dipalmitoyl-PC/dilauroyl-PC/cholesterol: nanoscopic domain formation driven by cholesterol. *Biophys. J.* 80:2775–2788.
7. Zhao, J., J. Wu, …, G. W. Feigenson. 2007. Phase studies of model biomembranes: complex behavior of DSPC/DOPC/cholesterol. *Biochim. Biophys. Acta.* 1768:2764–2776.
8. Heberle, F. A., J. Wu, …, G. W. Feigenson. 2010. Comparison of three ternary lipid bilayer mixtures: FRET and ESR reveal nanodomains. *Biophys. J.* 99:3309–3318.
9. Konyakhina, T. M., J. Wu, …, G. W. Feigenson. 2013. Phase diagram of a 4-component lipid mixture: DSPC/DOPC/POPC/chol. *Biochim. Biophys. Acta.* 1828:2204–2214.
10. Konyakhina, T. M., S. L. Goh, …, G. W. Feigenson. 2011. Control of a nanoscopic-to-macroscopic transition: modulated phases in four-component DSPC/DOPC/POPC/Chol giant unilamellar vesicles. *Biophys. J.* 101:L8–L10.
11. Heberle, F. A., R. S. Petruzielo, …, J. Katsaras. 2013. Bilayer thickness mismatch controls domain size in model membranes. *J. Am. Chem. Soc.* 135:6853–6859.
12. de Wit, G., J. S. H. Danial, …, M. I. Wallace. 2015. Dynamic label-free imaging of lipid nanodomains. *Proc. Natl. Acad. Sci. USA.* 112:12299–12303.
13. Goh, S. L., J. J. Amazon, and G. W. Feigenson. 2013. Toward a better raft model: modulated phases in the four-component bilayer, DSPC/DOPC/POPC/CHOL. *Biophys. J.* 104:853–862.
14. Lee, D. W., Y. Min, …, J. A. Zasadzinski. 2011. Relating domain size distribution to line tension and molecular dipole density in model cytoplasmic myelin lipid monolayers. *Proc. Natl. Acad. Sci. USA.* 108:9425–9430.
15. García-Sáez, A. J., S. Chiantia, and P. Schwille. 2007. Effect of line tension on the lateral organization of lipid membranes. *J. Biol. Chem.* 282:33537–33544.
16. Amazon, J. J., S. L. Goh, and G. W. Feigenson. 2013. Competition between line tension and curvature stabilizes modulated phase patterns on the surface of giant unilamellar vesicles: a simulation study. *Phys. Rev. E Stat. Nonlin. Soft Matter Phys.* 87:022708.
17. Kingsley, P. B., and G. W. Feigenson. 1979. The synthesis of a perdeuterated phospholipid: 1,2-dimyristoyl-*sn*-glycero-3-phosphocholine-d72. *Chem. Phys. Lipids.* 24:135–147.

18. Gleason, N. J., V. V. Vostrikov, …, R. E. Koeppe, 2nd. 2012. Tyrosine replacing tryptophan as an anchor in GWALP peptides. *Biochemistry.* 51:2044–2053.
19. Angelova, M., S. Soleau, and P. Méléard. 1992. Preparation of giant vesicles by external AC electric fields. Kinetics and applications. *Trends Colloid and Interface Sci. VI.* 89:127–131.
20. Baumgart, T., G. Hunt, …, G. W. Feigenson. 2007. Fluorescence probe partitioning between Lo/Ld phases in lipid membranes. *Biochim. Biophys. Acta.* 1768:2182–2194.
21. Morales-Penningston, N. F., J. Wu, …, G. W. Feigenson. 2010. GUV preparation and imaging: minimizing artifacts. *Biochim. Biophys. Acta.* 1798:1324–1332.
22. Petruzielo, R. S., F. A. Heberle, …, G. W. Feigenson. 2013. Phase behavior and domain size in sphingomyelin-containing lipid bilayers. *Biochim. Biophys. Acta.* 1828:1302–1313.
23. Esposito, C., A. Tian, …, T. Baumgart. 2007. Flicker spectroscopy of thermal lipid bilayer domain boundary fluctuations. *Biophys. J.* 93:3169–3181.
24. Pécréaux, J., H. G. Döbereiner, …, P. Bassereau. 2004. Refined contour analysis of giant unilamellar vesicles. *Eur. Phys. J. E Soft Matter.* 13:277–290.
25. Gracià, R. S., N. Bezlyepkina, …, R. Dimova. 2010. Effect of cholesterol on the rigidity of saturated and unsaturated membranes: fluctuation and electrodeformation analysis of giant vesicles. *Soft Matter.* 6:1472.
26. Budil, D. E., S. Lee, …, J. H. Freed. 1996. Nonlinear-least-squares analysis of slow-motion EPR spectra in one and two dimensions using a modified Levenberg-Marquardt algorithm. *J. Magn. Reson. A.* 120:155–189.
27. Ge, M., and J. H. Freed. 1999. Electron-spin resonance study of aggregation of gramicidin in dipalmitoylphosphatidylcholine bilayers and hydrophobic mismatch. *Biophys. J.* 76:264–280.
28. Dzikovski, B., and J. Freed. 2013. Membrane Fluidity. *In* Encyclopedia of Biophysics. G. C. K. Roberts, editor. Springer, Berlin, Germany, pp. 1440–1446.
29. Buboltz, J. T., and G. W. Feigenson. 1999. A novel strategy for the preparation of liposomes: rapid solvent exchange. *Biochim. Biophys. Acta.* 1417:232–245.
30. Amazon, J. J., and G. W. Feigenson. 2014. Lattice simulations of phase morphology on lipid bilayers: renormalization, membrane shape, and electrostatic dipole interactions. *Phys. Rev. E Stat. Nonlin. Soft Matter Phys.* 89:022702.
31. McConnell, H. M. 1991. Structures and transitions in lipid monolayers at the air-water interface. *Annu. Rev. Phys. Chem.* 42:171–195.
32. Zhou, F., and K. Schulten. 1995. Molecular dynamics study of a membrane-water interface. *J. Phys. Chem.* 99:2194–2207.
33. Kučerka, N., J. Pencer, …, J. Katsaras. 2007. Curvature effect on the structure of phospholipid bilayers. *Langmuir.* 23:1292–1299.
34. Arnold, O., J. C. Bilheux, …, J. Zikovsky. 2014. Mantid—data analysis and visualization package for neutron scattering and μ SR experiments. *Nucl. Instrum. Methods Phys. Res. Sect. A Accel. Spectrom. Detect. Assoc. Equip.* 764:156–166.
35. Pan, J., F. A. Heberle, …, J. Katsaras. 2013. Using small-angle neutron scattering to detect nanoscopic lipid domains. *Chem. Phys. Lipids.* 170–171:19–32.
36. Ackerman, D. G., and G. W. Feigenson. 2015. Multiscale modeling of four-component lipid mixtures: domain composition, size, alignment, and properties of the phase interface. *J. Phys. Chem. B.* 119:4240–4250.
37. Qi, Y., H. I. Ingólfsson, …, W. Im. 2015. CHARMM-GUI Martini maker for coarse-grained simulations with the MARTINI force field. *J. Chem. Theory Comput.* 11:4486–4494.
38. Lee, J., X. Cheng, …, W. Im. 2016. CHARMM-GUI input generator for NAMD, GROMACS, AMBER, OpenMM, and CHARMM/OpenMM simulations using the CHARMM36 additive force field. *J. Chem. Theory Comput.* 12:405–413.
39. Brooks, B. R., C. L. Brooks, 3rd, …, M. Karplus. 2009. CHARMM: the biomolecular simulation program. *J. Comput. Chem.* 30:1545–1614.
40. Jo, S., T. Kim, …, W. Im. 2008. CHARMM-GUI: a web-based graphical user interface for CHARMM. *J. Comput. Chem.* 29:1859–1865.
41. Hess, B., C. Kutzner, …, E. Lindahl. 2008. GROMACS 4: algorithms for highly efficient, load-balanced, and scalable molecular simulation. *J. Chem. Theory Comput.* 4:435–447.
42. Marrink, S. J., H. J. Risselada, …, A. H. de Vries. 2007. The MARTINI force field: coarse grained model for biomolecular simulations. *J. Phys. Chem. B.* 111:7812–7824.
43. Monticelli, L., S. K. Kandasamy, …, S.-J. Marrink. 2008. The MARTINI coarse-grained force field: extension to proteins. *J. Chem. Theory Comput.* 4:819–834.
44. Melo, M. N., H. I. Ingólfsson, and S. J. Marrink. 2015. Parameters for MARTINI sterols and hopanoids based on a virtual-site description. *J. Chem. Phys.* 143:243152.
45. McGibbon, R. T., K. A. Beauchamp, …, V. S. Pande. 2015. MDTraj: a modern open library for the analysis of molecular dynamics trajectories. *Biophys. J.* 109:1528–1532.
46. Marsh, D. 2009. Cholesterol-induced fluid membrane domains: a compendium of lipid-raft ternary phase diagrams. *Biochim. Biophys. Acta.* 1788:2114–2123.
47. Feigenson, G. W. 2009. Phase diagrams and lipid domains in multicomponent lipid bilayer mixtures. *Biochim. Biophys. Acta.* 1788:47–52.
48. Kučerka, N., M.-P. Nieh, and J. Katsaras. 2011. Fluid phase lipid areas and bilayer thicknesses of commonly used phosphatidylcholines as a function of temperature. *Biochim. Biophys. Acta.* 1808:2761–2771.
49. Kreutzberger, M. A., E. Tejada, …, P. F. Almeida. 2015. GUVs melt like LUVs: the large heat capacity of MLVs is not due to large size or small curvature. *Biophys. J.* 108:2619–2622.
50. Veatch, S. L., K. Gawrisch, and S. L. Keller. 2006. Closed-loop miscibility gap and quantitative tie-lines in ternary membranes containing diphytanoyl PC. *Biophys. J.* 90:4428–4436.
51. Uppamoochikkal, P., S. Tristram-Nagle, and J. F. Nagle. 2010. Orientation of tie-lines in the phase diagram of DOPC/DPPC/cholesterol model biomembranes. *Langmuir.* 26:17363–17368.
52. Kučerka, N., J. Gallová, …, J. Katsaras. 2009. Areas of monounsaturated diacylphosphatidylcholines. *Biophys. J.* 97:1926–1932.
53. Palmieri, B., and S. A. Safran. 2013. Hybrid lipids increase the probability of fluctuating nanodomains in mixed membranes. *Langmuir.* 29:5246–5261.
54. Heberle, F. A., M. Doktorova, …, G. W. Feigenson. 2013. Hybrid and nonhybrid lipids exert common effects on membrane raft size and morphology. *J. Am. Chem. Soc.* 135:14932–14935.
55. Konyakhina, T. M., and G. W. Feigenson. 2016. Phase diagram of a polyunsaturated lipid mixture: brain sphingomyelin/1-stearoyl-2-docosahexaenoyl-*sn*-glycero-3-phosphocholine/cholesterol. *Biochim. Biophys. Acta.* 1858:153–161.
56. Baykal-Caglar, E., E. Hassan-Zadeh, …, J. Huang. 2012. Preparation of giant unilamellar vesicles from damp lipid film for better lipid compositional uniformity. *Biochim. Biophys. Acta.* 1818:2598–2604.
57. Ackerman, D. G., and G. W. Feigenson. 2016. Effects of transmembrane α-helix length and concentration on phase behavior in four-component lipid mixtures: a molecular dynamics study. *J. Phys. Chem. B.* 120:4064–4077.
58. Pan, J., T. T. Mills, …, J. F. Nagle. 2008. Cholesterol perturbs lipid bilayers nonuniversally. *Phys. Rev. Lett.* 100:198103.
59. Marsh, D. 2006. Elastic curvature constants of lipid monolayers and bilayers. *Chem. Phys. Lipids.* 144:146–159.
60. Gawrisch, K., D. Ruston, …, N. Fuller. 1992. Membrane dipole potentials, hydration forces, and the ordering of water at membrane surfaces. *Biophys. J.* 61:1213–1223.
61. Travesset, A. 2006. Effect of dipolar moments in domain sizes of lipid bilayers and monolayers. *J. Chem. Phys.* 125:084905.

Biophysical Journal, Volume *112*

Supplemental Information

Line Tension Controls Liquid-Disordered + Liquid-Ordered Domain Size Transition in Lipid Bilayers

Rebecca D. Usery, Thais A. Enoki, Sanjula P. Wickramasinghe, Michael D. Weiner, Wen-Chyan Tsai, Mary B. Kim, Shu Wang, Thomas L. Torng, David G. Ackerman, Frederick A. Heberle, John Katsaras, and Gerald W. Feigenson

SUPPORTING MATERIAL

This supporting material contains detailed protocols and controls used in the experimental and theoretical procedure.

1. Line tension measurements

1. 1. Sample Preparation and cooling procedure

For ρ window measurements, samples contained 0.02 mol% C12:0 DiI; GUVs were made by electroformation with several modifications (1). The lipid films that formed after evaporation in vacuum were swelled at 45°C (when containing bSM, eSM or pSM) or 55°C (when containing DSPC) in 100 mM sucrose under a 5 Hz AC field for 2 h to form the GUVs. To measure ρ windows, the slides were cooled to room temperature (21°C) over 10 h and the vesicles harvested into 100 mM glucose solution in glass test tubes. Samples rested for ~ 1 h so that the sucrose-containing GUVs could settle through the less dense glucose solution. This procedure removes lipid debris, hence background signal, from the GUVs.

To measure line tension, samples contained 0.2 mol% C12:0 DiI, and GUVs were formed as above but were cooled in two different ways to form domains of a suitable size as described in the main text. For low ρ values, circular lipid domains with ~5 μm diameter were obtained by cooling GUVs from 50 to 23°C over ~ 3 h. For higher ρ values, very large round Ld + Lo domains formed over several hours, so the necessary smaller round domains were obtained by faster cooling. In detail, room temperature GUV samples were reheated briefly to 50°C, then 3-4 μl of the sample was deposited into the slide chamber maintained at either room temperature or cooled prior to sample deposition, depending on what was required to obtain ~5 μm diameter domains. Before imaging, GUVs were allowed to settle for 5 minutes on the microscope slide. Circular lipid domains with ~5-μm diameter were then studied at 23°C. The cooling procedure for each sample is summarized in Table S1, followed by a more detailed description of each protocol.

TABLE S1 Fast cooling techniques used in different four-lipid systems

Four-lipid systems	Composition	ρ values	Fast cooling setup
DSPC/DPhPC+DLPC/chol	0.5/0.23/0.27	0-0.2	Immediately visualized
		0.3-0.6	Heated up to 45^{o}C and quickly cooled to 23^{o}C
		0.8-1.0	Heated up to 45^{o}C and quickly cooled to 0^{o}C
DSPC/DOPC/POPC/chol	0.39/0.39/0.22	0-06	Cooled to room temperature over 10 hours, re-heated up to 50^{o}C and quickly cooled to room temperature
DSPC/DPhPC/POPC/chol	0.39/0.39/0.22	0-0.3	Cooled to room temperature over 10 hours, re-heated up to 50^{o}C and quickly cooled to room temperature
bSM/DOPC+POPC/chol	0.39/0.39/0.22	0.5-0.7	Cooled to room temperature over 10 hours and re-heated up to 50^{o}C and quickly cooled to 0^{o}C

		0.8-1.0	Cooled to room temperature over 10 hours, re-heated up to 50°C and quickly cooled to room temperature
eSM/DOPC+POPC/chol	0.39/0.39/0.22	0.1-0.2	Cooled over 3.5 hours + Heated up to 50°C and quickly cooled to room temperature
		0.3-1.0	Cooled to room temperature over 10 hours and re-heated up to 50°C and quickly cooled
pSM/DOPC+POPC/chol	0.39/0.39/0.22	0.0-0.05	Cooled over 3.5 hours
		0.1-1.0	Cooled to room temperature over 10 hours and re-heated up to 50°C and quickly cooled to room temperature
bSM/DOPC+POPC/chol + 4mol% WALP	0.39/0.39/0.22	0.1-0.25	Cooled over 3.5 hours
		0.35-1.0	Cooled to room temperature over 10 hours and re-heated up to 50°C and quickly cooled to room temperature

Cooled to room temperature over 10 hours and re-heated to 50 °C and quickly cooled to 0 °C:
Cooled from 45 °C to room temperature over 10 hours and harvested into 100 mM glucose and allowed to settle. The samples were heated back up to 50 °C and then 2-3µl were placed on a slide that had been cooled to 0 °C. The slide was allowed to return to room temperature before imaging.

Heated up to 50 °C and quickly cooled to room temperature:
Cooled from 45 °C to room temperature over 10 hours and harvested into 100 mM glucose and allowed to settle. The samples were heated back up to 50 °C and then 2-3µl were placed on a slide and imaged without any further heating or cooling processes.

Cooled over 3.5 hours:
Cooled from 45 °C to room temperature over 3.5 hours and harvested into 100 mM glucose and allowed to settle. 3-4µl were placed on a slide and imaged without any further heating or cooling processes.

1. 2. Sample Compositions

Sample compositions for each mixture were chosen based on which compositions produced small isolated domains. These compositions are displayed in Table S2.

TABLE S2. Sample composition used in the line tension measurements for six different lipid mixtures.

Mixture	High-Tm	Low-Tm	chol
PSM/DOPC/POPC/chol	0.39	0.39	0.22
eSM/DOPC/POPC/chol	0.39	0.39	0.22
bSM/DOPC/POPC/chol	0.39	0.39	0.22
DSPC/DOPC/POPC/chol	0.55	0.20	0.25
DSPC/DPhPC/POPC/chol	0.45	0.30	0.25
DSPC/DPhPC/DLPC/chol	0.50	0.23	0.27

1. 3. Optimizing Probe Concentration

The short exposure times required to capture domain fluctuations for line tension measurements necessitate intense illumination and/or high probe concentration. The potential for light-induced artifacts increases with both of these parameters (2). To limit artifacts during the optimization of probe concentration and data collection, we used a four-component mixture of fully saturated lipids: DSPC/DPhPC/DLPC/chol. DPhPC, when it is the only low-Tm lipid, gives rise to macroscopic phase separation, whereas DLPC as the sole low-Tm lipid yields nanodomains. Here, ρ = DPhPC/ DPhPC+DLPC. Initial tests of probe concentration were carried out at the ρ value where macroscopic phase separation first occurs for this four-component mixture. Increasing concentrations of probes, LR-DOPE and 12:0 DiI, were tested to achieve the best balance of GUV yield and contrast. 0.2 mol% C12:0 DiI proved to be ideal for line tension measurements. Higher probe concentrations tended to reduce yield while at the same time increasing the likelihood of light induced artifacts.

1. 4. Data Acquisition and Analysis

All microscopy measurements used an inverted Nikon Eclipse TI-E (Nikon Instruments), with a 60x 1.2 NA water immersion objective, and additional 1.5x intermediate magnifier for line tension measurements. Excitation of DiI was via a Spectra X Light Engine (Lumencor, Inc.) with a green LED (542/27). To narrow the wavelengths of excitation and emission, we used a filter cube with 545/25 excitation filter and 605/70 emission filter. Images were acquired using a Zyla 5.5 sCMOS camera (Andor Tehcnology Ltd) with 6.4μm pixels. With a total of 90x magnification for line tension, each pixel represented ~71nm. Data acquisition and control of illumination intensity were performed using the software NIS-Elements Basic Research (MVI, Inc).

For reliable line tension measurements, we looked at the top center of a GUV for approximately-circular domains greater than 5 μm in diameter but less than $1/5^{th}$ of the diameter of the entire GUV (3). For each domain, we acquired a 15 s time series: 10 ms exposure times with a 30 ms cycle time, yielding ~500 frames. A minimum of 10 such domains were imaged for each ρ value. It was a challenge to find domains that were both circular and of a useful size and at the top of the GUV. For all four-component mixtures, we can only start to measure line tension at a ρ value where phase separation is visible under the light microscope and for which circular domains can form. This was often at a ρ value just slightly higher than that at the first appearance of macroscopic domains. To find such domains, we searched the sample using fluorescence at a low 2% illumination intensity of the Spectra X. Once a useful domain was found, data were collected at 50% illumination intensity. During the acquisition, the Spectra X was

triggered by the camera so that the LED was only on during the 10 ms exposure time. During the 20 ms between frames, the LED was off. This reduced light exposure, minimizing light-induced artifacts.

Analysis of domain fluctuations was implemented using Matlab 2010a and followed the basic methodology of Baumgart et al (3). The software located domain boundaries throughout a time series using Matlab's Canny edge detection, taking the largest boundary to define the domain of interest (Fig. S1). A domain in a particular frame was only considered for analysis ("valid") when it was approximately circular and within 3% of the original domain area. The average Fourier transform of the valid boundaries was then used to calculate σ for each mode using Eq. 1 from the main text. The line tension of a domain was taken to be the average σ over modes $n = 2 – 5$. Averages were only considered valid if the time series had more than ~ 250 valid frames and produced relatively constant values of σ over modes $n = 2 – 5$.

We used only modes 2-5 for the analysis in part because they were shown by Baumgart et al. to effectively measure line tension, and also because we empirically found them to accurately measure line tensions in fluctuating domain simulations analogous to those described in Baumgart et al (3).

Evidence that this method works is shown in Fig. S1, where it is straightforward to see the differences in measured line tension for domains at low and high ρ. For bSM/DOPC/POPC/chol, macroscopic phase separation is first observed at $\rho \sim 0.50$ with a line tension value of 0.29 ± 0.04 pN (Fig. S1 *A*, *B*). At $\rho = 1.00$, the line tension is 1.3 ± 0.1 pN (Fig. S1 *C*, *D*). The greater fluctuation amplitudes visible in A and B are consistent with lower line tensions compared to C and D.

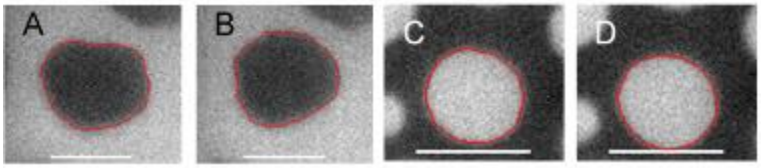

Fig. S1**.** Snapshots of domains over time, with detected boundaries outlined in red, show differences in line tension. A,B) Domain at $\rho = 0.5$ with an average line tension of 0.29 ± 0.04 pN. The time between A and B is ~ 0.75 s. C,D) Domain at $\rho = 1.00$ with line tension 1.31 ± 0.12 pN. The time between C and D is ~ 0.75 s. Scale bars are 5 μm.

1.5. Testing for light-induced effects on line tension

Since the dye concentration of 0.2% is rather high in order to achieve the required contrast, there is a possibility of light-induced artifacts. These can result in the break-up of domains, the fusion of domains, or a change in the amplitude and frequency of the fluctuations of the domains. Therefore, we always test for any light-induced artifacts by measuring the change in line tension over time. For each domain, the data were split into successive subsets of 100 frames (successive subsets of 3 s time intervals); the first subset containing data from time 0-3 s, the second subset containing data from time 3-6 s, etc. For a given domain, the line tension value for each subset was normalized to the line tension value in the first 100 frames. These data were then averaged together over all domains at each ρ value (Fig. S2). While there were some fluctuations in the normalized line tensions, most ρ values exhibited no illumination- or time-dependent trends. For DSPC/DOPC/POPC/chol, at $\rho = 0.2$, Fig. S2 shows a decrease in line tension by nearly 50% from the first subset to the second, for instance. This unreliable change is considered to be due to light induced artifacts, and this kind of data was then discarded. This composition was carefully remeasured to avoid light induced artifacts.

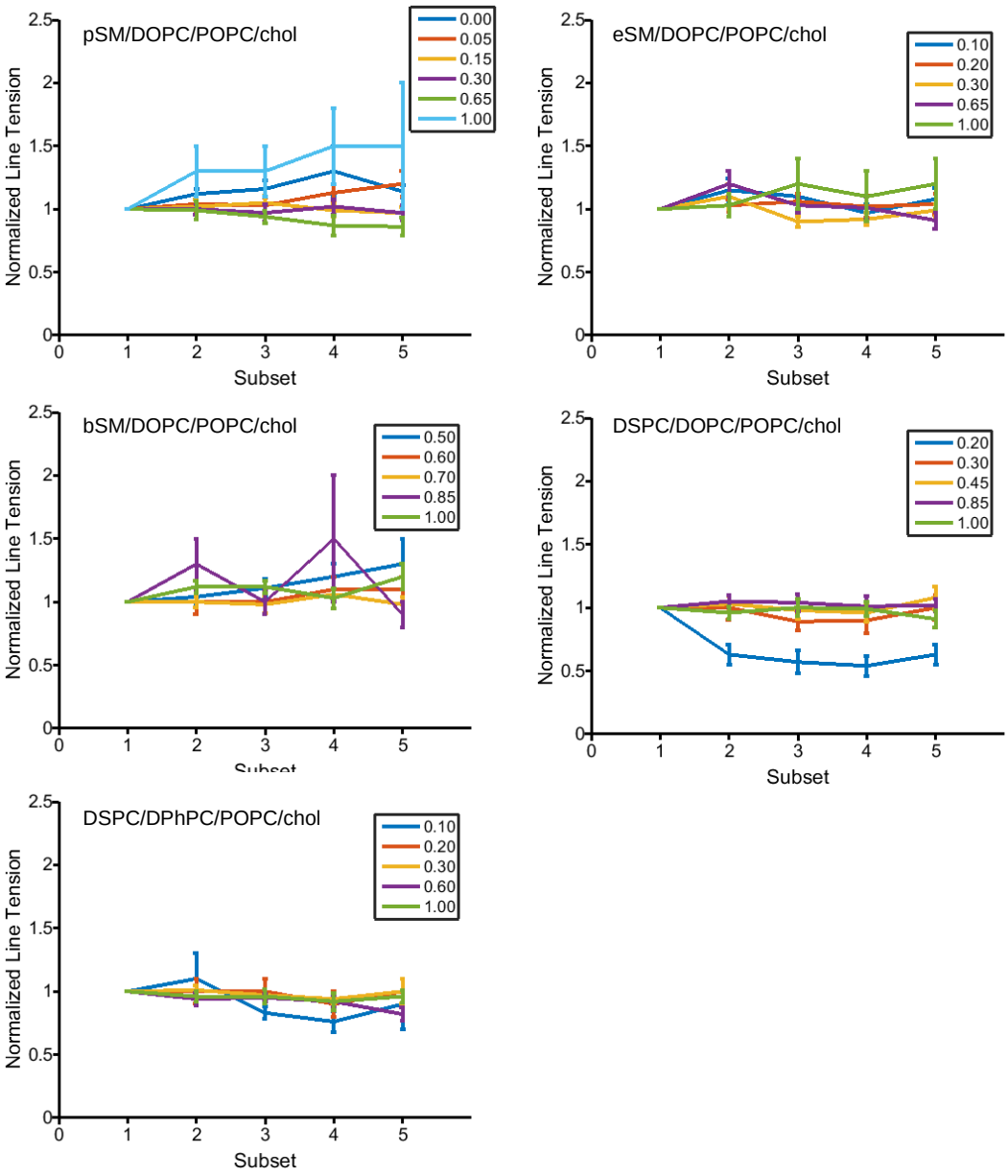

Fig. S2**.** Light-induced effects can be detected by measuring line tension over time. For these tests, an average line tension of each successive subset of 100 frames is normalized by the line tension in the first 100 frames. The legend indicates the system's ρ value.

The effect of such light-induced artifacts can be clearly seen in Fig. S3, where we show a single domain at this composition throughout its 15 s exposure. While the domain starts off round, by 15 s, its shape is very irregular. This data was discarded.

We note that for each of the 6 mixtures studied, the trend in line tension versus ρ was similar for each subset. This, together with the fact that most ρ values show no trend in line tension over time, allows us to conclude that light-induced effects were negligible.

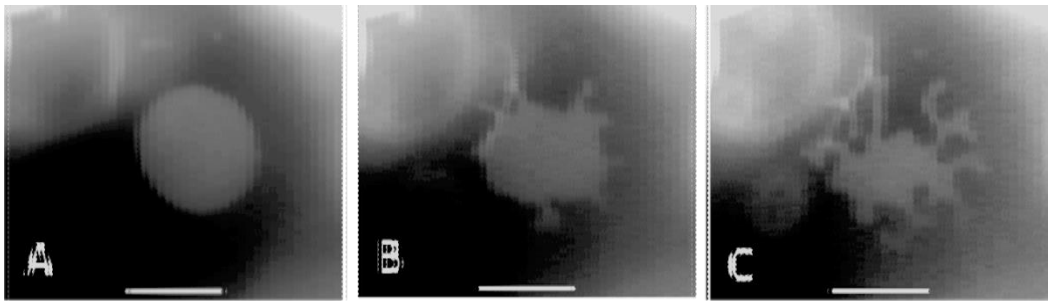

Fig. S3**.** Domain exhibiting light induced artifacts. Domain at ρ = 0.2 for DSPC/DOPC/POPC/chol, at A) t = 0 s, B) t = ~ 7.5 s, and C) t = ~15 s. This domain was not used for analysis, but shows how a round domain can become misshapen over time due to illumination. Scale bars are 5 μm.

1.6. Cooling Controls

To ensure that the measured line tension values did not differ based on the cooling method used — slow cooling over 3.5 hours or fast cooling over a few seconds — the pSM/DOPC/POPC/chol and eSM/DOPC/POPC/chol systems were imaged after making samples using both cooling protocols. Since different methods of cooling were required to obtain suitable domains for different ρ values, only a few ρ values for the pSM and eSM could be imaged using *both* methods of cooling. The line tension values observed show that the values of the line tension are within the standard error of each other and follow similar trends regardless of slower or faster cooling method (Fig. S4). The line tension values shown in the main text are the values obtained from domains using both cooling methods.

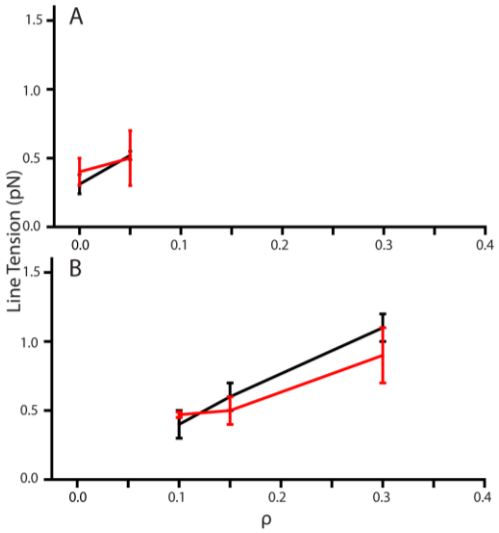

Fig. S4**.** Line tension measurements using faster (black) or slower cooling (red) are the same for A) pSM/DOPC/POPC/chol and B) eSM/DOPC/POPC/chol. Error bars: mean ± standard error.

1. 7. Size Dependence Controls

GUV and domain radii were recorded for all measurements. To ensure that the line tension measurement itself does not depend on the size of the domain or the size of the GUV it is on, we have compared normalized line tension to size, where line tensions were normalized to the average line tension for a given composition. In Fig. S5 *A* it can be seen that the normalized line tensions remain close to one,

meaning that line tension is independent of domain radius. Similarly, line tension is independent of GUV radius as shown in Fig. S5 *B*. The ratio of domain size to GUV size is another factor that could cause a distortion in measured line tension, but importantly, for the domains used in this study, the line tension measurement is independent of this ratio (Fig. S5 *C*).

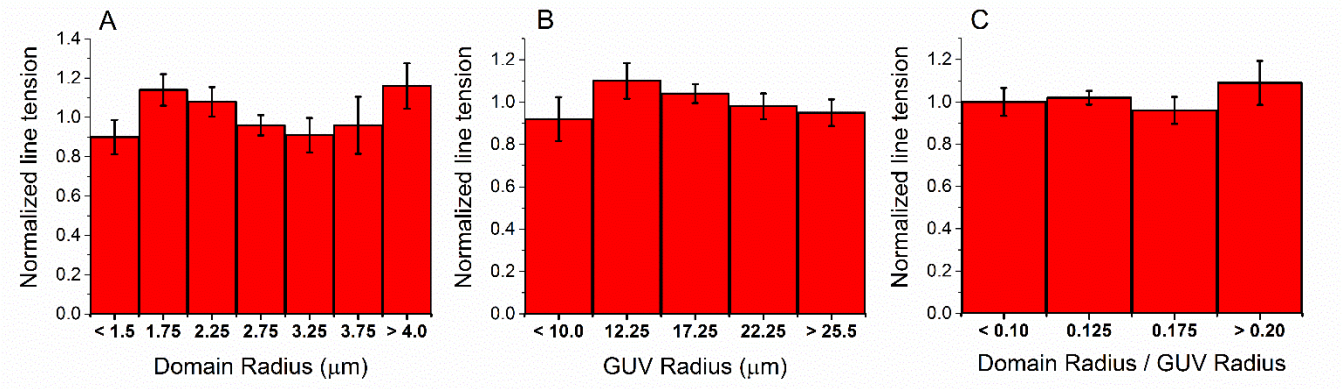

Fig. S5. DSPC/DPhPC/DLPC/chol line tension is independent of domain size and GUV size. At each ρ value each line tension measurement was normalized to the average of all measurements at that ρ value. Normalized line tension was compared to domain radius (A), to GUV radius (B) and to the ratio of the two (C). Bars reflect bins of approximately equal size.

2. Small Angle Neutron Scattering (SANS)

SANS $I(q)$ data were analyzed with a coarse-grained Monte Carlo method described in Heberle et al. (4). Briefly, vesicles were modeled as spherical shells of radius R_v and thickness t_{ac} corresponding to the hydrophobic thickness of the bilayer, with polydispersity assumed to follow a Schulz distribution (5). The shell volume was divided into one or more randomly placed, non-overlapping circular domains of radius R_d. Random points were generated within the shell volume in proportion to the neutron scattering length density (NSLD) contrast of the bilayer phases with the surrounding water using a rejection algorithm (*i.e.*, points were uniformly generated within the shell and tested for inclusion in a domain until both phases accumulated the desired number of points). The NSLD-weighted pair distance distribution $P(r)$ was calculated from the set of random points, and the procedure was repeated for 10^5 vesicles to obtain an ensemble average. The scattering intensity was then calculated as (6):

$$I(q) = 4\pi \int_0^\infty P(r) \frac{\sin qr}{qr} dr. \qquad \text{(S1)}$$

For best S/N in SANS measurements we used compositions where area fractions of Ld and Lo were nearly equal. Most trajectories for line tension measurements used the same compositions. Samples were prepared near the lowest-chol tieline of the Ld + Lo region where the compositions of the coexisting phases are well determined, which is a necessity for the bending energy and ESR experiments.

We explored a wider range of LUV size at a single ρ value to find any influence on measured nanodomain size. Fig. S6 shows domain sizes at ρ = 0 for DSPC/POPC/chol, obtained from extruded vesicles with nominal extrusion pore sizes ranging from 30 – 200 nm diameter (Fig. S6, open squares). Extrusion of neutral lipids using pore sizes ≥ 100 nm is known to generate a minor population of

paucilamellar vesicles (PLVs) that can be eliminated by adding a small fraction of charged lipid to the mixture (7). To test whether Bragg scattering from contaminating PLVs might affect the determination of domain size, samples were also prepared in which 5 mol% of each PC lipid was replaced with its PG counterpart (Fig. S6, diamonds). Within measurement uncertainty, domain size has a negligible dependence on vesicle size at $\rho = 0$: all measured domain radii fall in the range 5.0 – 6.8 nm. The presence of 5 mol% PG resulted in a ~5% decrease in domain size (Fig. S6).

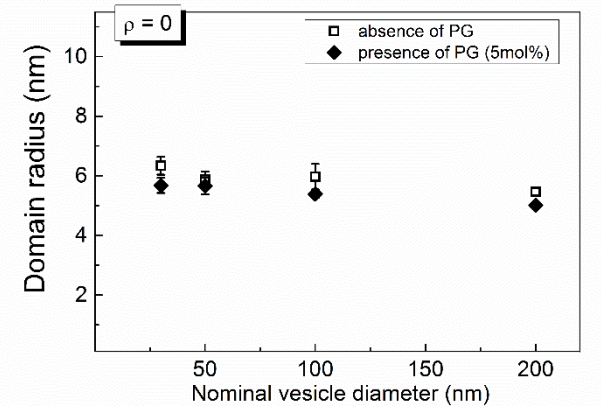

Fig. S6. SANS reveals that nanodomain size is independent of vesicle size. Domain radii obtained from Monte Carlo modeling of SANS data for LUVs composed of DSPC/POPC/chol = 39/39/22. At this $\rho = 0$ composition, the domain radius is independent of vesicle size and does not change significantly upon addition of 5 mol% charged lipid.

Discussion of Nanoscopic Phase Separation

As we discuss in detail in the main text, properties of Ld and Lo phases, such as bending energy, order parameter, rotational diffusion, and probe partitioning between phases gradually change on either side of the dramatic domain size transition and change rather little through the transition itself. In this sense the size transition does not have the hallmarks of a phase transition (8).

Previous experimental observations are consistent with Ld + Lo nanoscopic domains being phase separated mixtures. These mixtures were found to have all of the same phase coexistence regions as mixtures that show macroscopic domains. Indeed, the formation of Lo phase from Lβ phase occurs at $\chi chol \approx 0.16$ in all the mixtures we have studied, leading to similarities for different lipid mixtures in this region of the phase diagram (9–11). Of particular importance is the finding that the high-chol "upper" boundary of the Ld + Lβ coexistence region in a Gibbs Triangle phase diagram is a straight line in composition space in all the mixtures we have studied (9–11). This is readily explained if the region above Ld + Lβ is a three-phase coexistence triangle of Ld + Lβ + Lo, which has been directly verified for a macroscopic mixture by fluorescence microscopy observations (12). Because the Ld + Lβ upper boundary is linear in nanoscopic mixtures (10, 11), there is no critical point, consistent with an adjacent 3-phase region. In turn, this three-phase region must, according to the Phase Rule, be adjacent to a region with either four or two phases, inconsistent with this region being a one-phase microemulsion. Further, Goh et al. measured the areas of the modulated phase domains in GUVs and found the observed area fractions to follow the Lever-Arm Rule. This implies that the uniform surround must itself be a single phase, otherwise the Lever-Arm Rule would fail to describe the area fractions.

3. Molecular Dynamics (MD) simulations

Fig. S7 displays the full bilayer of a 20,000-lipid MD simulation at three ρ values: 0.5, 0.65, and 0.8. Each is displayed after phase separation, and the increasing size and connectivity of domains is visible as ρ increases. This increase in size and connectivity means a decrease in interface length between two phases, consistent with rising line tension. A 30 nm x 30 nm portion of the ρ = 0.65 plot (Fig. S7 *B*) which contains a single nanodomain is shown in the main body of this paper and was run for 3.6 μs. The other simulations represent the system after 1.2 μs. The additional time was found to not change phase morphology, implying 1.2 μs is sufficient for equilibration.

Any analysis on such a system depends on how we define a phase in a simulation. In order to prevent very small patches of one or a few lipids from being classified as domains, an adjustment was implemented: If a majority of a given lipid's nearest neighbors including itself were classified in the first round as being in a particular phase, the lipid was assigned to that phase in the second round. Our method is but one of several based on measuring local enrichment of high-Tm lipid (13, 14). A choice to compare neighboring phases twice is somewhat arbitrary but serves to remove clusters too small to be considered domains. Otherwise, the nonrandom clustering of lipids representing a small component of a phase can be mislabeled. A test of k-means clustering based on local composition revealed nearly identical classifications of lipids into phases. A further study of a large bilayer over a long time scale (> 10 μs), while computationally expensive, would provide further detail into the time-dependent properties of nanodomains, including their changing perimeters and whether individual domains form or disappear in a system already at equilibrium.

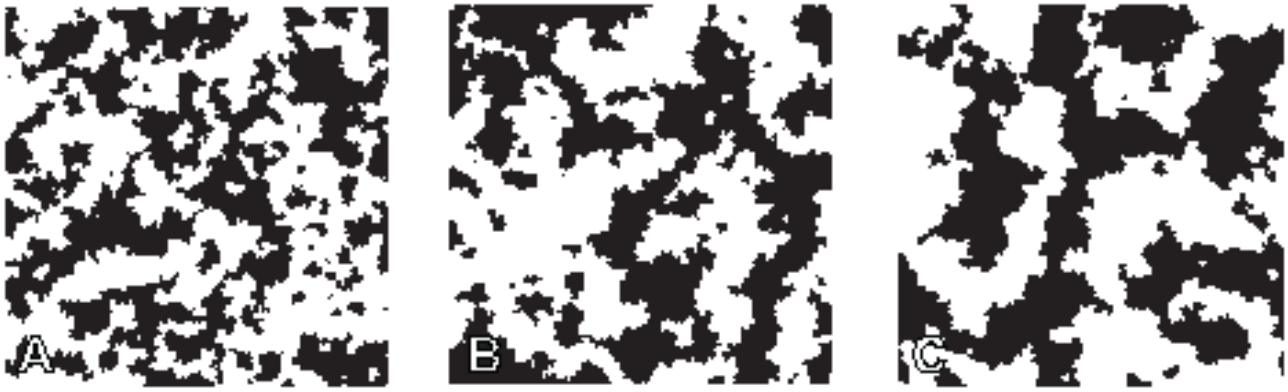

Fig. S7 Size and connectivity of domains increases as ρ increases. Lo is shown is black, and Ld is shown in white. Panels depict increasing ρ with (A) ρ = 0.5, (B) ρ = 0.65, and (C) ρ = 0.8. The visible decrease in interface length is consistent with rising line tension. Each simulation has a box size of approximately 74 nm x 74 nm.

Our Molecular Dynamics movie (included with this Supporting Material in a separate file, named MD_nanodomains.avi) demonstrates the dynamic shape and evolution of nanodomains. It shows the progression of a single 4-component system as it develops during phase separation and then continues rearranging. The time progression reveals the complex, non-circular morphology of a domain and its fluctuating nature. Lipids are colored by type (DUPC in blue, PUPC in cyan, DPPC in red, and cholesterol in yellow). Phases are not marked, but the formation of patches rich in DPPC and cholesterol (red and yellow) clearly shows the formation of Lo domains.

4. Bending Modulus measurement for DSPC/DOPC/POPC/chol

4.1. Sample composition

Bending modulus measurements were performed in DSPC/DOPC/POPC/chol using the lipid composition of Ld phase, DSPC/(DOPC+POPC)/chol = 0.10/0.80/0.10, or Lo phase, as described in Table S3. It should be noted that the right hand side of DSPC/DOPC/POPC/chol phase diagram changes with ρ. Therefore, the lipid composition used in Lo measurements smoothly change.

TABLE S3. Sample composition used in bending modulus measurements, showing only Lo phase of DSPC/DOPC/POPC/chol.

ρ	DSPC	(DOPC+POPC)	chol
0	0.58	0.17	0.25
0.2	0.62	0.11	0.26
0.35	0.64	0.09	0.27
0.6	0.67	0.06	0.28
0.8	0.67	0.05	0.28
1	0.68	0.04	0.28

4.2. Analysis Methods and Validation

Fig. S8 shows an example of edge detection and the bilayer fluctuations. For these experiments, a 4% difference in osmolality between inner and outer solutions was created, yielding slightly flaccid vesicles suitable for the measurement. Given the density difference of the solutions, vesicles with radii > 20 μm were excluded to avoid significant distortion due to gravity (15). Vesicles of radii < 10μm have too few pixels defining the contour, leading to poor statistics, and thus were also excluded. Only vesicles exhibiting visible fluctuations and free of defects like tethers, buds, or attachments were imaged. Vesicles contained 0.02 mol% C12 DiI to enable line scans of fluorescent dye intensity to identify and exclude multilayered vesicles.

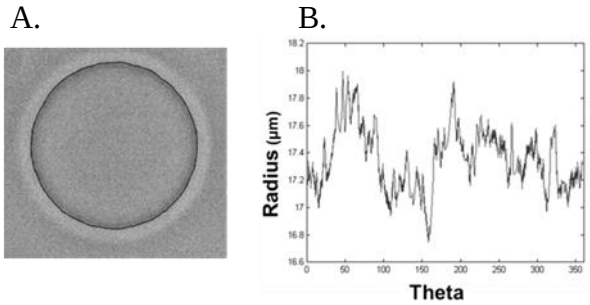

Fig. S8. Fluctuation Spectroscopy Edge Detection. (A) Fluctuations were observed with phase contrast images of the vesicle equator. Contour as defined by Canny edge detection is superimposed in black. (B) Fluctuation spectrum from the contour shown, where theta refers to points on the quasi-circular contour.

Our method for measuring bending moduli closely followed the methods of Gracià et al. (16). Our determination of the range of useful mode numbers hinged on the following considerations: Tension predominates for low modes, and high modes become indistinguishable from noise. Thus an intermediate range of modes, numbers 10 to 20, provides a reliable measure of the bending modulus (16). Measurements which did not result in a plateau of these modes were considered unreliable and excluded from the composition average.

To determine appropriate exposure times, we analyzed the relaxation time of various modes according to: $(4\,\eta\,R^3)/(\kappa_c m^3)$, where η is viscosity, R is radius, κ is the bending modulus, and m is the mode number (17). We determined that 1 ms is an adequate exposure time for the range of bending moduli in our experiments. The Spectra X white light source used for these experiments was triggered by the camera and remained off for 29 ms of the 30 ms cycle time used. Each dataset per vesicle measured included 1600 exposures. Achieving sufficient contrast requires moderately intense light, so we investigated the possibility of light-induced artifacts. For each measurement, datasets were divided into 200-frame subsets. No trends in these subsets were observed (data not shown). We confirmed that our procedure yields values similar to the bending moduli obtained by others (16, 18).

5. Single-Dye Fluorescence Trajectories

5.1. Phase Diagram and Sample Trajectories

Fig. S9 shows the phase diagram for bSM/POPC/chol (ρ = 0) and bSM/DOPC/chol (ρ = 1) and the lipid composition of 61 samples prepared along a thermodynamic tieline (two-phase region). These phase diagrams in Fig. S9 are similar to the ones reported in Ref. (11), but here we updated the boundaries somewhat with new measurements. For the intermediate trajectories obtained for ρ = 0.4 and ρ = 0.75, we interpolated the phase boundaries linearly with ρ. The Kp determination depends on the Lo and Ld phase fractions. The inserted axis in the phase diagram displays the fraction of Lo phase, χ_{Lo}, which represents the independent variable of Eq. (S3) below. The arrows labeled 1 and 2 point to phase boundaries of the coexistence region and represent pure Ld and Lo phases, respectively.

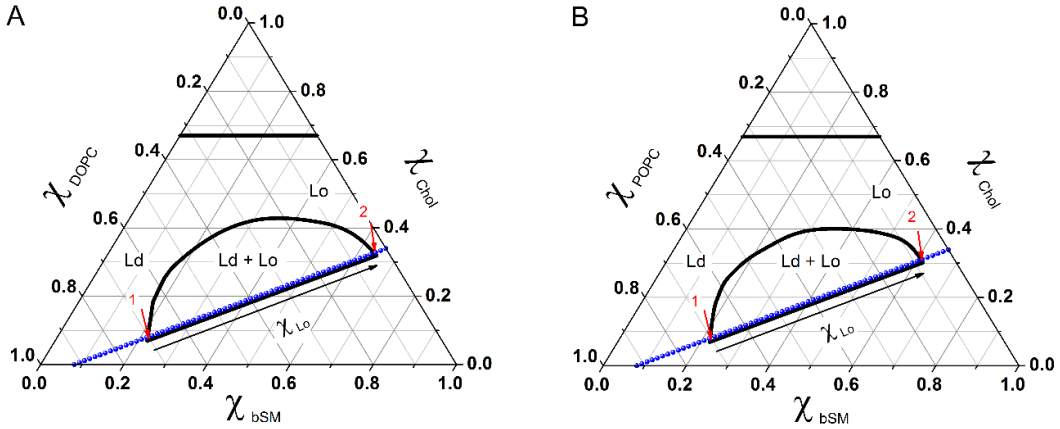

Fig. S9. Phase diagram of (A) bSM/POPC/chol (ρ = 0) and (B) bSM/DOPC/chol (ρ = 1). Sample trajectories were prepared with the lipid compositions shown in the phase diagram (blue). The inserted axis in the phase diagram displays the fraction of Lo phase, χ_{Lo}, and the arrows labeled 1 and 2 point to the phase boundaries of the coexistence region.

5.2. Quenching Correction

For the fluorescence trajectories, dyes were used at a concentration that does not exhibit large self-quenching effects, as displayed in Fig. S10. This study of fluorescence self-quenching is also important for quenching corrections if necessary.

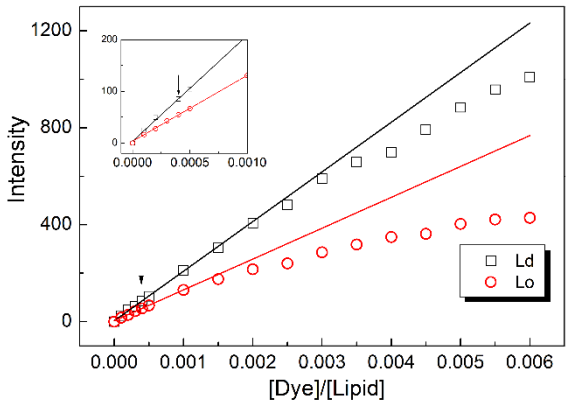

Fig. S10. Fluorescence self-quenching with increasing dye concentration. The self-quenching curve of Bodipy-PC for bSM/DOPC/chol in Ld and Lo phases (composition labeled 1 and 2, respectively, Fig. S9 *A*) is shown. The inset shows the linearity of Intensity and [dye]/[lipid] at low [dye]/[lipid] ratios. The small arrow displayed in the graph points to the [dye]/[lipid]=1/2500 ratio used in the fluorescence experiments.

5.3. Partition Coefficient Analysis

Fig. S11 shows the fluorescence trajectory for bSM/POPC/chol ($\rho = 0$) (also displayed in the inset of Fig. 5). The data were fitted using Eq. S3 below, where χ_{Lo} is the fraction of Lo phase, as shown in Fig. S9.

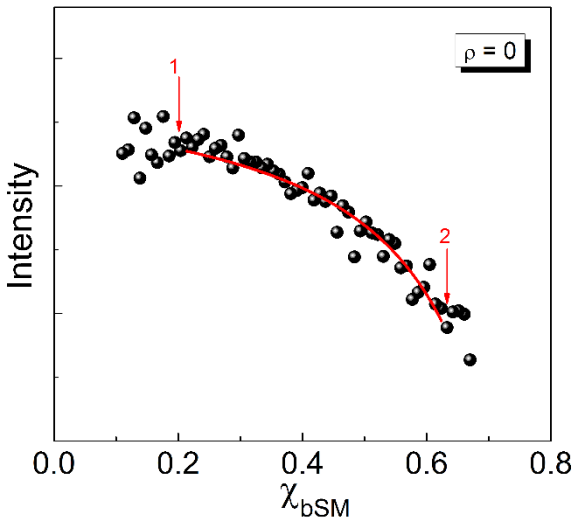

Fig. S11. Fluorescence emission of Bodipy-PC in bSM/POPC/chol. The lipid composition of each sample is displayed in the tieline of Fig. S9. The single dye fluorescence (corrected for quenching effects) was analyzed according to Eq. (S2).

The single dye fluorescence along a tieline is given by

$$F = \frac{F_{Ld}\, Kp\,(1-\chi_{Lo})+F_{Lo}\,\chi_{Lo}}{Kp\,(1-\chi_{Lo})+\,\chi_{Lo}} \quad \text{(S2)}$$

where F_{Ld} and F_{Lo} are the fluorescence signals from pure Ld and Lo phases, (i.e. the fluorescence at the lipid compositions represented by 1 and 2 in Fig. S11). The partition coefficient is defined by

$$Kp \equiv \frac{n_{Ld}/\chi Ld}{n_{Lo}/\chi Lo} \quad \text{(S3)}$$

such that Kp > 1 indicates partitioning that favors the Ld phase, and n_{Ld} and n_{Lo} indicate the fraction of dye in Ld and Lo phase, respectively. The error bars displayed in the Figure 5A were calculated by the goodness of fit of Eq. (S2).

6. Probe Partition Coefficient Determination for GUVs

We used line scans in GUV snapshots to measure the fluorescence intensity ratio between Ld and Lo phases. ImageJ was used to analyze snapshots and record intensity profiles. The intensity ratio between Ld and Lo phases was calculated using the area under the peak in the intensity profiles after subtracting the background intensity. Here, we performed 10 line scans for each phase in a single GUV, and we repeated this procedure for 5-10 different GUVs.

Bodipy-PC is intrinsically brighter in Ld phase compared to Lo phase. It is well known that fluorescent dyes can have different quantum yield (intensities) in different environments (19). Here, we have corrected the intensity ratio between Ld and Lo phases, obtained from the line scans, for the intrinsic fluorescence of the dye in each single phase.

In addition, the partition coefficient obtained by fluorescence trajectories is related to the total fluorescence that comes from Lo and Ld phases. This quantification differs from a single measurement of fluorescent intensity in Ld and Lo phases, as obtained from the line scans. Therefore, in order to compare the partition coefficient obtained using these two different techniques of fluorescence trajectories and fluorescence microscopy, we considered in our calculations that the Lo phase occupies 30% less area than the Ld phase (20, 21), in order to account for the total intensities from Ld and Lo, observed in the GUVs studies.

Fig. S12 displays an example of the partition coefficient measurement in GUVs. The snapshot in Fig. S12 *A* represents a typical line scan of Ld and Lo phases. Fig. S12 *B* displays the 10 different line scans for each phase used in the calculations of the partition coefficient. The error bars displayed in Figure 5A for Kp measurements on GUVs correspond to standard error of 5-10 GUVs, with 10 line scans for each phase.

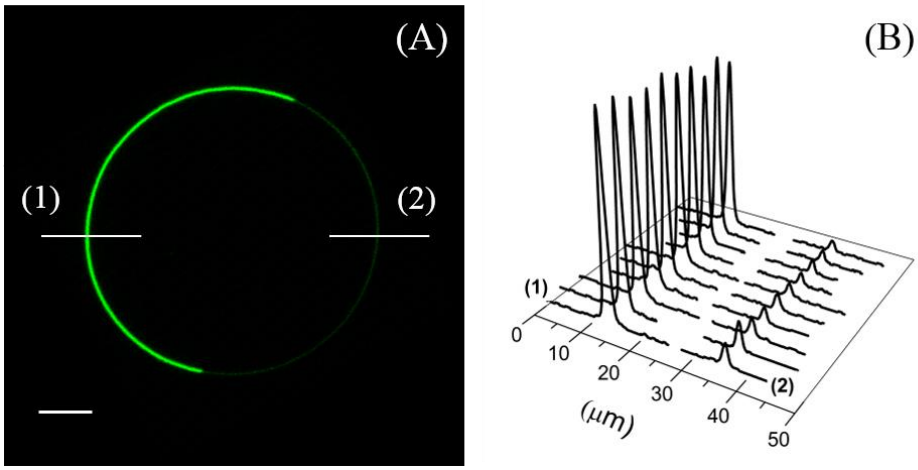

Fig. S12. Intensity profile measurements on GUVs. GUV lipid composition bSM/(DOPC+POPC)/chol = 0.4/0.4/0.2, dye/lipid = 1/2500. (A) Snapshot of a GUV, which exhibits Ld (brighter) and Lo phase separation. Lines labeled by the numbers (1) and (2) are line scans obtained in Ld and Lo phase, respectively. (B) Examples of 10 different line scans measured along Ld (brighter) and Lo phases. Scale bar: 5 μm.

7. Electron spin resonance (ESR)

The ESR spectrum of 111 samples measured along ρ for DSPC/DOPC/POPC/chol were analyzed according to equation:

$$S(\rho) = (1 - n_{Lo}) * Ld(\rho) + n_{Lo} * Lo(\rho) \qquad \text{(S4)}$$

where *Ld(ρ)* and *Lo(ρ)* correspond to the characteristic spectrum of Ld and Lo phase for a certain value of ρ, and $n_{Ld} = (1 - n_{Lo})$ and n_{Lo} represent the fractions of paramagnetic probe in Ld and Lo phase, respectively. Additionally, the characteristic spectra of Ld and Lo phases can be written as a linear combination of the spectra measured in ρ = 0 (DSPC/POPC/chol) and ρ = 1 (DSPC/DOPC/chol), according to Eqs. S5 and S6.

$$Ld(\rho) = (1 - \rho) * Ld(0) + \rho * Ld(1) \qquad \text{(S5)}$$

$$Lo(\rho) = (1 - \rho) * Lo(0) + \rho * Lo(1) \qquad \text{(S6)}$$

The partition coefficient is defined according to Eq. S3, except in this case n_{Ld} and n_{Lo} refer to the fraction of 16PC spin label. As mentioned above, χLd and χLo are the fractions of Ld and Lo phase.

Fig. S13 shows the spectra of (A) Ld phase and (B) Lo phase, for ρ = 0, 0.3 and 1. These spectra represent the phase morphologies of nano domains, modulated phases and macro domains, respectively. We observed small changes in the ESR spectra along ρ reflecting small changes in the order parameter and the rotational diffusion as shown in Table 1.

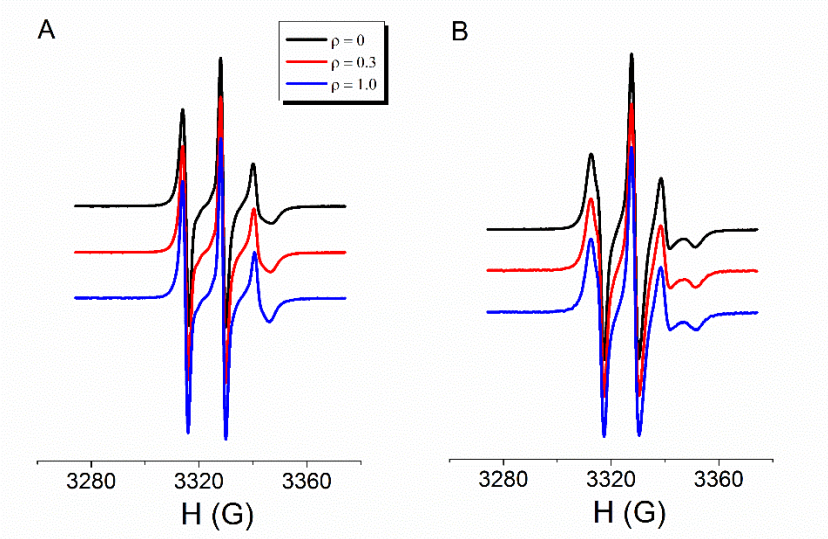

Fig. S13 ESR Spectra change little along ρ for both Ld and Lo. (A) Ld phase spectra. (B) Lo phase spectra. ρ = 0 is shown in black, 0.3 in red and 1in blue. Spectra are shifted for clarity.

8. Dipole-Dipole Repulsion Model

In order to explore the implications of dipole repulsion for domain size, we model the total energy of a phase-separated bilayer as a sum of a phase boundary energy from line tension that scales with domain perimeter and an electrostatic potential energy arising from permanent lipid dipoles.

An initial question for these studies is whether dipoles in one leaflet would have their fields largely cancelled by the opposing dipoles in the other leaflet. This does occur for the methyl dipoles that give rise to long-range repulsion in lipid monolayers (22). The dipoles of interest in this study would be farther apart, as shown in Fig. S14, suggesting that the oppositely oriented dipoles would not cancel. This was conclusively shown in the calculations described below and in the main text, wherein two leaflets of oppositely oriented dipoles produce a net repulsive electrostatic interaction when their magnitude and separation distance is comparable to carbonyl groups in a lipid bilayer.

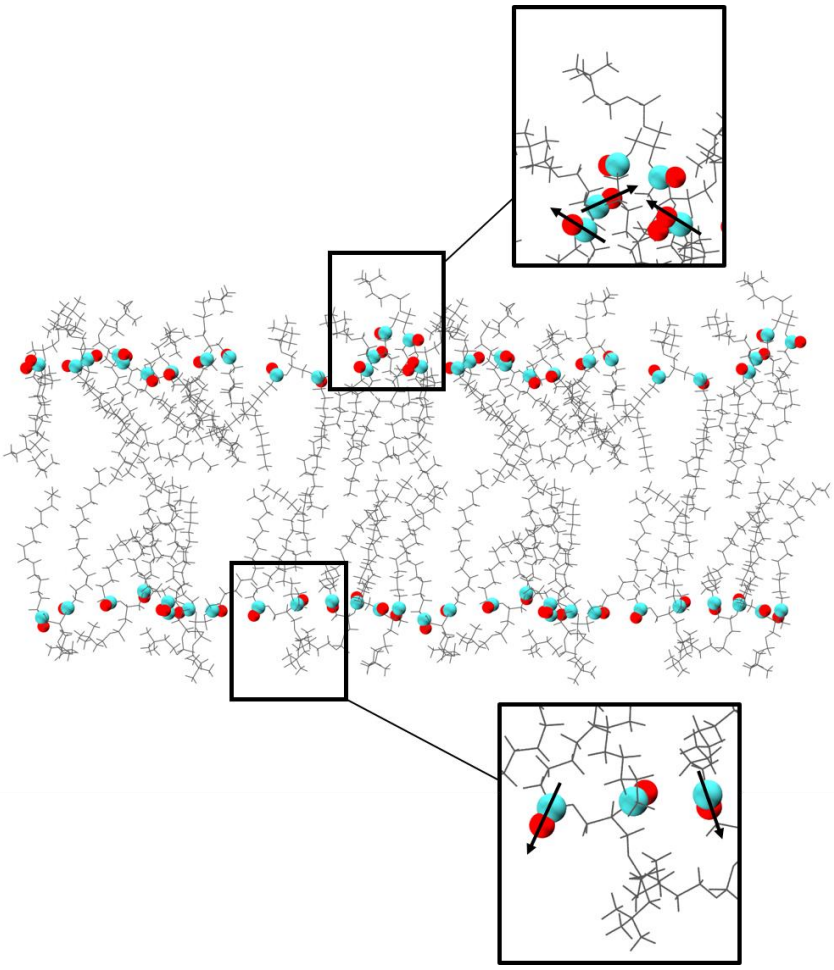

Fig. S14. The direction and location of carbonyl dipoles in a bilayer. Carbonyl groups at the top of each acyl chain are presented as spheres (cyan for carbon and red for oxygen), while the rest of the phospholipid is presented as gray lines. Dipoles drawn pointing from the positive carbon toward the negative oxygen along the bond reveal that the net dipole moment of each leaflet is normal to the bilayer and pointed outward toward the water (inset) and that there is individual variation in the dipole alignment. Phospholipids are displayed in each leaflet as a representation of a system obtained from Molecular Dynamics simulations of a DPPC bilayer.

For the calculations, we needed to determine the energetically favorable domain size for a set of lipid parameters. We therefore chose a fixed total domain area α and varied the number of domains N_D into which that area was divided; assuming circular domains, the domain radius is given by $R_D = \sqrt{\alpha/(\pi N_D)}$. The energetically favorable domain size R_D^* is defined as that which results in the lowest energy for a given set of parameters defined below.

The energetic contribution from the line tension σ is given by $2\pi R_D N_D \sigma$. To determine the electrostatic contribution, we first considered the electrostatic potential energy for an arbitrary arrangement of discrete dipoles in a membrane:

$$V = \frac{1}{4\pi\varepsilon\varepsilon_0}\sum_{i=1}^{N_L-1}\sum_{j=i+1}^{N_L}\left[\frac{\overrightarrow{\boldsymbol{p_i}}\cdot\overrightarrow{\boldsymbol{p_j}}}{\left\|\overrightarrow{\boldsymbol{r_{ij}}}\right\|^3} - \frac{3\left(\overrightarrow{\boldsymbol{p_i}}\cdot\overrightarrow{\boldsymbol{r_{ij}}}\right)\left(\overrightarrow{\boldsymbol{p_j}}\cdot\overrightarrow{\boldsymbol{r_{ij}}}\right)}{\left\|\overrightarrow{\boldsymbol{r_{ij}}}\right\|^5}\right], \qquad (S7)$$

where ε_0 is the permittivity of free space, ε is the dielectric constant (here, the dielectric constant of the bilayer region near the dipoles), N_L is the number of dipoles (here, the number of lipids possessing a permanent dipole), $\overrightarrow{\boldsymbol{p_i}}$ are the dipole moment vectors, $\overrightarrow{\boldsymbol{r_{ij}}}$ are the vectors connecting a pair of dipoles, and $\left\|\overrightarrow{\boldsymbol{r_{ij}}}\right\|$ are the distances between these dipole pairs. For lipids distributed identically in the two bilayer leaflets and dipoles aligned with the bilayer normal, the total electrostatic potential energy of the bilayer is a sum of intra- and interleaflet contributions, i.e. $V_{total} = 2V_{intra} + V_{inter}$, with

$$V_{intra} = \frac{1}{4\pi\varepsilon\varepsilon_0}\sum_{i=1}^{N_L^{top}-1}\sum_{j=i+1}^{N_L^{top}}\left(\frac{(p_i p_j)^2}{\left\|\overrightarrow{\boldsymbol{r_{ij}}}\right\|^3}\right), \qquad (S8)$$

$$V_{inter} = \frac{1}{4\pi\varepsilon\varepsilon_0}\sum_{i=1}^{N_L^{top}}\sum_{j=1}^{N_L^{bot}}\left(\frac{3(hp_i p_j)^2}{\left\|\overrightarrow{\boldsymbol{r_{ij}}}\right\|^5} - \frac{(p_i p_j)^2}{\left\|\overrightarrow{\boldsymbol{r_{ij}}}\right\|^3}\right). \qquad (S9)$$

Here, N_L^{top} and N_L^{bot} are the number of lipids in the top and bottom leaflets (with one net permanent dipole assigned to each), h is the bilayer thickness, and p_i are the dipole magnitudes. To simplify the calculations, we assumed that the domain and its surround differed only in the magnitudes of their dipoles, and that the main effect of electrostatics on domain size was due to the difference in dipole magnitudes between domain and surround, rather than their absolute values. With these assumptions, we set $p_{sur} = 0$, and replaced p_{dom} with $\Delta\phi\varepsilon\varepsilon_0 A_L$, where $\Delta\phi$ is the electrostatic potential difference between the domain and surround and A_L is the area per lipid in the domain. Our final simplification was to assume that domains are far enough apart that inter-domain energies are negligible. The total intra- and interleaflet contributions can then be rewritten as:

$$V_{intra} = \frac{N_D}{4\pi\varepsilon\varepsilon_0}\sum_{i=1}^{N_L^{top}-1}\sum_{j=i+1}^{N_L^{top}}\left(\frac{(\Delta\phi\varepsilon\varepsilon_0 A_L)^2}{\left\|\overrightarrow{\boldsymbol{r_{ij}}}\right\|^3}\right), \qquad (S10)$$

$$V_{inter} = \frac{N_D}{4\pi\varepsilon\varepsilon_0}\sum_{i=1}^{N_L^{top}}\sum_{j=1}^{N_L^{bot}}\left(\frac{3(h\Delta\phi\varepsilon\varepsilon_0 A_L)^2}{\left\|\overrightarrow{\boldsymbol{r_{ij}}}\right\|^5} - \frac{(\Delta\phi\varepsilon\varepsilon_0 A_L)^2}{\left\|\overrightarrow{\boldsymbol{r_{ij}}}\right\|^3}\right), \qquad (S11)$$

where N_L^{top} and N_L^{bot} now refer to lipid dipoles within a single domain.

In the continuum limit, as described in the main text, the discrete summations are replaced by integrals:

$$V_{intra} = N_D \frac{1}{2} \frac{{N_L}^2}{4\pi\varepsilon\varepsilon_0} \int_a^{2R_D} \frac{(\Delta\phi\varepsilon\varepsilon_0 A_L)^2}{r^3} P(r, R_D) dr, \qquad (S12)$$

$$V_{inter} = N_D \frac{{N_L}^2}{4\pi\varepsilon\varepsilon_0} \int_0^{2R_D} \left[\frac{3(h\Delta\phi\varepsilon\varepsilon_0 A_L)^2}{(h^2 + r^2)^{5/2}} - \frac{(\Delta\phi\varepsilon\varepsilon_0 A_L)^2}{(h^2 + r^2)^{3/2}} \right] P(r, R_D) dr, \qquad (S13)$$

where $a = 2\sqrt{A_L/\pi}$ (the lower limit of the V_{intra} integral) is the distance of closest approach between two dipoles, N_L is the total number of lipid dipoles in one domain leaflet, and $P(r, R_D)$ is the distribution of dipole separation distances derived as follows. Considering a vector $\boldsymbol{v} = (r\sin\theta, r\cos\theta)$ contained within the domain, the probability density for all vectors of magnitude r is proportional both to r, and to the overlap area A of two disks of radius R_D whose centers are separated by a distance r, as shown by the shaded region in Fig. S15*a*. This area is given by:

$$A(r, R_D) = 4 \int_{r/2}^{R_D} dx \sqrt{R_D - x^2} = 2{R_D}^2 \tan^{-1}\left[\frac{R_D}{r} \sqrt{4 - \left(\frac{r}{R_D}\right)^2} \right] - \frac{rR_D}{2} \sqrt{4 - \left(\frac{r}{R_D}\right)^2}. \qquad (S14)$$

The normalized probability distribution is then given by:

$$P(r, R_D) = \frac{rA(r, R_D)}{\int_0^{2R_D} rA(r, R_D) dr} = \frac{r}{\pi {R_D}^3} \left\{ 4R_D \tan^{-1}\left[\frac{R_D}{r} \sqrt{4 - (r/R_D)^2} \right] - r\sqrt{4 - (r/R_D)^2} \right\}. \qquad (S15)$$

Fig. S15*b* plots Eq. S15 for R_D = 10 (solid blue line), as well as a histogram of pair-distances obtained by generating 10^4 random points within a disk of radius 10, demonstrating the validity of the analytical solution.

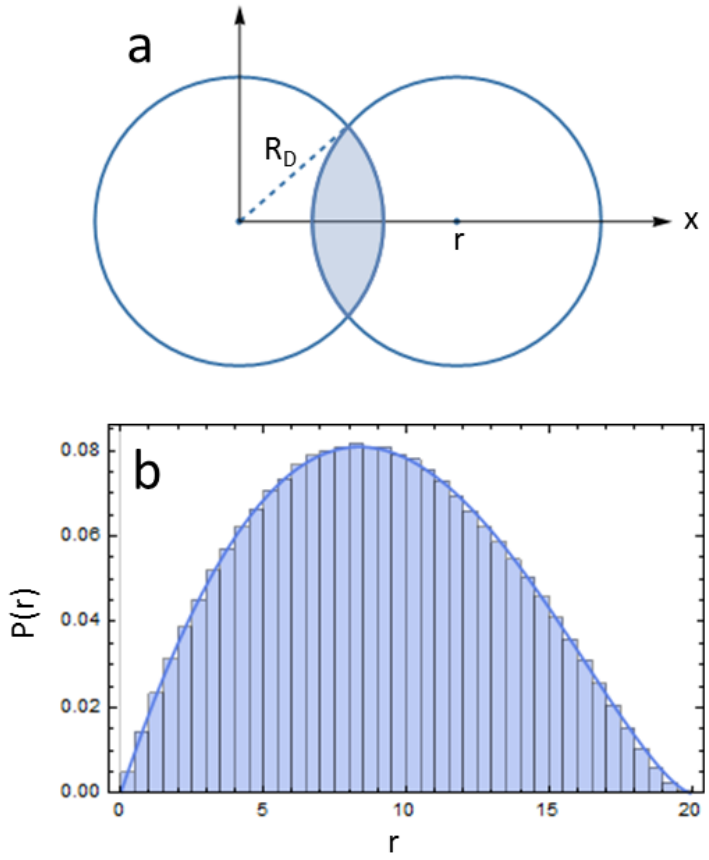

Fig. S15. Analytical solution for the pair-distance distribution function of a disk. *a*, geometric interpretation of the density of vectors of magnitude r contained with a disk of radius R_D as an overlap area. *b*, Eq. S15 plotted for R_D = 10 (solid blue line) and a corresponding pair-distance histogram generated from random points as described in the text, demonstrating the validity of the analytical solution.

For the calculations presented in the main text, we chose parameters reasonable for model bilayer membranes: $\varepsilon = 8$, $A_L = 60$ Å^2, $h = 3$ nm, $\Delta\phi$= 0.1 or 0.2 V, and total domain area $\alpha = \pi\ 30^2$ μm^2, corresponding to a single domain with a 30 μm radius.

In addition to the dipole continuum model discussed in the main text, we also calculated equilibrium domain sizes using three related models:

1. Modeling more explicitly the SANS experiment, we calculated the energetically favorable domain size for circular domains within a 60 nm diameter spherical vesicle; domain and surrounding membrane were assigned continuous dipole distributions with dipole potentials of 1 V and 0.9 V respectively, giving a dipole difference $\Delta\phi = 0.1$ V, or $\Delta\phi = 0.2$ V as in the isolated domain continuum model of the main text. Monte Carlo sampling was then used to calculate the distance distributions within domain and surround and between domain and surround, from which the electrostatic potential was calculated. The total domain area was fixed at 40% of the vesicle surface for this and the remaining two models.

2. We calculated the energetically favorable domain size as in the main text, but using discrete dipoles rather than the continuum limit. Within the circular domain, dipoles were assigned a magnitude of $0.1\ V * (\varepsilon\varepsilon_0 A_L) = 1.0617$ Debye and distributed approximately uniformly using a Matlab script (23).

3. We replaced the above discrete dipoles with discrete positive and negative charges calculated from the aforementioned dipole magnitude, assuming a dipole length of 1.23 Å (a typical carbonyl bond length), yielding charge magnitudes of ~ 0.18 e^-. In each model, h, ε and A_L are the same as in the main text.

For all models, we fixed the total domain area and chose reasonable values for membrane electrostatic properties, varying only the number of domains. For the three models discussed above, computational limitations prevent accessing arbitrarily large domain sizes: for these models, we chose a bilayer surface area corresponding to a ~ 60 nm diameter vesicle that resulted in a single "macrodomain" limit of R_d ~ 40 nm (to facilitate comparison, we also applied the continuum model to this case).

All four models reveal a sharp transition from many smaller domains, to a single large domain that is limited only by the vesicle size, with increasing line tension. Moreover, for all four models this transition occurs at similar values of line tension. Slight differences between the models are also evident. For example, treating the systems continuously versus discretely results in small differences in the line tension value required to induce the domain size transition. The stepwise nature of the vesicle continuum model arises due to computational limitations in fully sampling all possible numbers of domains, and the steps in the discrete models arises from the constraint that the number of dipoles per domain must be an integer value. Nevertheless, the four models are in good agreement over the range of accessible parameter space. Especially importantly, each model predicts an abrupt domain size transition at intermediate line tensions, indicating that continuum models can faithfully reproduce the discretization of real membranes. Despite differences in the models, we find that the vesicle model produces results which agree with the simplified continuum model, thus supporting the analysis methodologies and assumptions of the main text (namely that the main electrostatic effect is due to differences in electrostatic potential between domain and surround such that the surround can be ignored in favor of more simple analyses involving a flat, isolated domain). These models also show that the nature of the two competing interactions of line tension and electrostatics favor an abrupt transition in domain size and are not sensitive to the exact values used in the models until they take on unphysically large or small values (Figs. S16 and S17 described further below).

8.2 Model Sensitivity

As mentioned in the main text, the precise line tension value where the domain size transition occurs is sensitive to the choice of model parameters. However, the finding of an abrupt transition is robust, occurring for a wide range of parameter values as described below.

We investigated the influence of the parameters displayed in Table S4 by independently varying each parameter in the calculations. Fig. S16 plots the equilibrium domain radius as a function of the line tension for different values of dielectric constant, $\boldsymbol{\varepsilon}$, while holding other parameter values ($\boldsymbol{A_L}$, $\boldsymbol{h}$ and $\Delta\boldsymbol{\phi}$) constant as displayed in Table S4.

Table S4. Parameters used in the dipole-dipole repulsion simulations.

Parameter	Canonical value	Description
$\boldsymbol{\varepsilon}$	8	Dielectric constant
$\boldsymbol{\Delta\phi}$	0.2 V	Dipole potential difference between domain and surrounding phases
$\boldsymbol{h}$	3.0 nm	Separation distance between dipole planes in opposing leaflets
$\boldsymbol{A_L}$	60 Å^2	Area per dipole

For convenience, we label the line tension value where the domain size transition occurs as λ*. We found that, upon increasing the dielectric constant, the line tension value required to form macroscopic domains decreased, as displayed in Fig. S16. This result is physically intuitive, since an increase in the dielectric constant should decrease the influence of electrostatics.

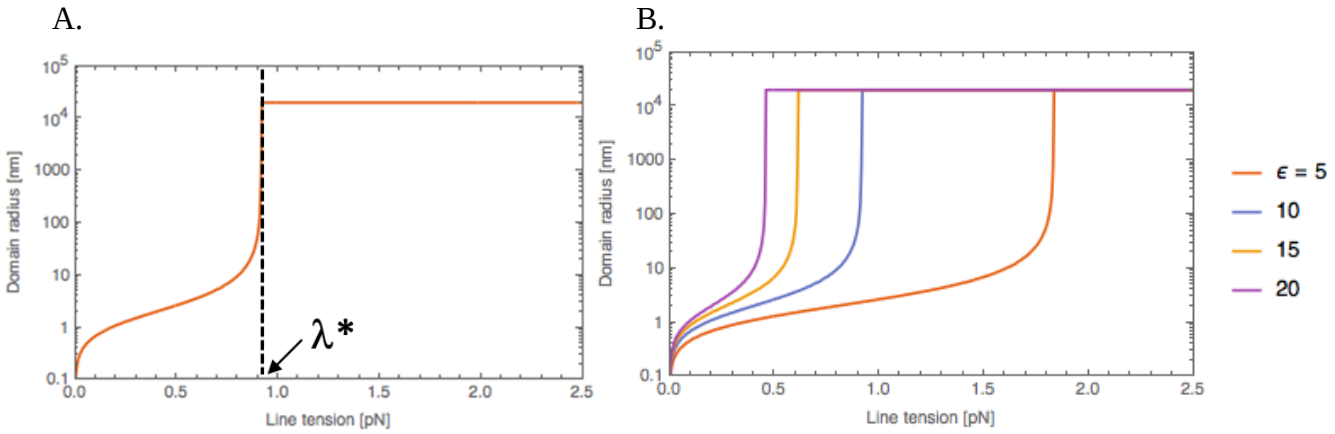

Fig. S16. Sensitivity of the continuum model to dielectric constant. (A) For a given parameter set, we define **λ*** as the line tension value where domain size reaches its limiting macroscopic value. (B) Increasing the dielectric constant over a reasonable range while holding other parameter values constant at their "canonical" values (Table S4) shifts the domain size transition to lower line tensions as the effects of electrostatics are diminished. In addition, we calculated **λ*** as a function of each individual parameter– ε, A_L, h and $\Delta\phi$ –while all other parameters were fixed, with the results shown in Fig. S17.

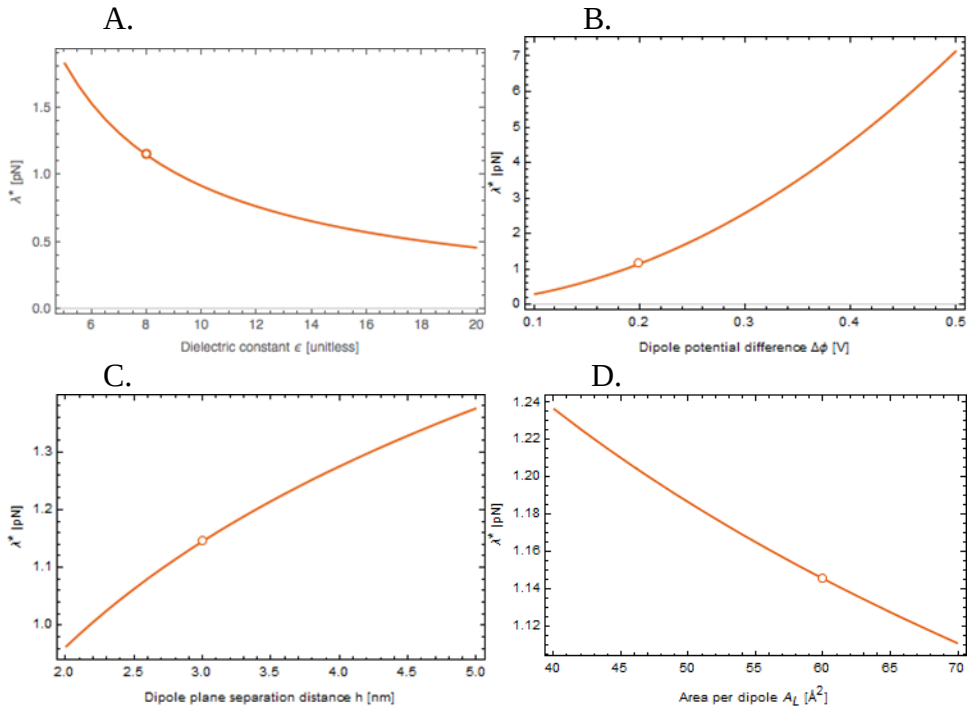

Fig. S17. Sensitivity of the continuum model to parameter values. (A) Varying the dielectric constant, ε, (at fixed dipole magnitude) over the range 5-20 results in critical line tension values from 0.45-1.8 pN (4-fold variation). (B) Varying the dipole potential difference, Δϕ, over the range 0.1-0.5 V results in critical line tension values from 0.2-7 pN (35-fold variation). (C) Varying the dipole plane separation distance, h, over the range 2-5 nm results in critical line tension values from 0.9-1.4 pN (1.5-fold variation). (D) Varying the area per dipole, A_L, over the range 40-70 Å^2 results in critical line tension values from 1.1-1.25 pN (1.1-fold variation). Open circle depicts **λ***, corresponding to the canonical parameters.

9. References

1. Angelova, M., S. Soleau, and P. Méléard. 1992. Preparation of giant vesicles by external AC electric fields. Kinetics and applications. Trends Colloid …. 89: 127–131.
2. Morales-Penningston, N.F., J. Wu, E.R. Farkas, S.L. Goh, T.M. Konyakhina, J.Y. Zheng, W.W. Webb, and G.W. Feigenson. 2010. GUV preparation and imaging: minimizing artifacts. Biochim. Biophys. Acta. 1798: 1324–32.
3. Esposito, C., A. Tian, S. Melamed, C. Johnson, S.-Y. Tee, and T. Baumgart. 2007. Flicker spectroscopy of thermal lipid bilayer domain boundary fluctuations. Biophys. J. 93: 3169–3181.
4. Heberle, F.A., R.S. Petruzielo, J. Pan, P. Drazba, N. Kučerka, R.F. Standaert, G.W. Feigenson, and J. Katsaras. 2013. Bilayer thickness mismatch controls domain size in model membranes. J. Am. Chem. Soc. 135: 6853–9.
5. Heberle, F.A., V.N.P. Anghel, and J. Katsaras. 2015. Scattering from phase-separated vesicles. I. An analytical form factor for multiple static domains. J. Appl. Crystallogr. 48: 1391–1404.
6. Feigin, L.A., and D.I. Svergun. 1987. Structure Analysis by Small-Angle X-Ray and Neutron Scattering. Boston, MA: Springer US.
7. Kučerka, N., J. Pencer, J.N. Sachs, J.F. Nagle, and J. Katsaras. 2007. Curvature Effect on the Structure of Phospholipid Bilayers. Langmuir. 23: 1292–1299.

8. Denbigh, K. 1981. The Principles of Chemical Equilibrium. Fourth. Cambridge University Press.
9. Heberle, F.A., J. Wu, S.L. Goh, R.S. Petruzielo, and G.W. Feigenson. 2010. Comparison of three ternary lipid bilayer mixtures: FRET and ESR reveal nanodomains. Biophys. J. 99: 3309–18.
10. Konyakhina, T.M., J. Wu, J.D. Mastroianni, F.A. Heberle, and G.W. Feigenson. 2013. Phase diagram of a 4-component lipid mixture: DSPC/DOPC/POPC/chol. Biochim. Biophys. Acta. 1828: 2204–14.
11. Petruzielo, R.S., F.A. Heberle, P. Drazba, J. Katsaras, and G.W. Feigenson. 2013. Phase behavior and domain size in sphingomyelin-containing lipid bilayers. Biochim. Biophys. Acta. 1828: 1302–13.
12. Zhao, J., J. Wu, F. a Heberle, T.T. Mills, P. Klawitter, G. Huang, G. Costanza, and G.W. Feigenson. 2007. Phase studies of model biomembranes: complex behavior of DSPC/DOPC/cholesterol. Biochim. Biophys. Acta. 1768: 2764–76.
13. Sodt, A.J., M.L. Sandar, K. Gawrisch, R.W. Pastor, and E. Lyman. 2014. The Molecular Structure of the Liquid-Ordered Phase of Lipid Bilayers. J. Am. Chem. Soc. 136: 725–732.
14. Ackerman, D.G., and G.W. Feigenson. 2015. Multiscale modeling of four-component lipid mixtures: Domain composition, size, alignment, and properties of the phase interface. J. Phys. Chem. B. 119.
15. Henriksen, J.R., and J.H. Ipsen. 2002. Thermal undulations of quasi-spherical vesicles stabilized by gravity. Eur. Phys. J. E. Soft Matter. 9: 365–74.
16. Gracià, R.S., N. Bezlyepkina, R.L. Knorr, R. Lipowsky, and R. Dimova. 2010. Effect of cholesterol on the rigidity of saturated and unsaturated membranes: fluctuation and electrodeformation analysis of giant vesicles. Soft Matter. 6: 1472.
17. Méléard, P., T. Pott, H. Bouvrais, and J.H. Ipsen. 2011. Advantages of statistical analysis of giant vesicle flickering for bending elasticity measurements. Eur. Phys. J. E. 34: 116.
18. Pécréaux, J., H.G. Döbereiner, J. Prost, J.F. Joanny, and P. Bassereau. 2004. Refined contour analysis of giant unilamellar vesicles. Eur. Phys. J. E. 13: 277–290.
19. Lakowicz, J.R. 2006. Principles of Fluorescence Spectroscopy Principles of Fluorescence Spectroscopy. .
20. Mills, T.T., G.E.S. Toombes, S. Tristram-Nagle, D.-M. Smilgies, G.W. Feigenson, and J.F. Nagle. 2008. Order parameters and areas in fluid-phase oriented lipid membranes using wide angle X-ray scattering. Biophys. J. 95: 669–81.
21. Alwarawrah, M., J. Dai, and J. Huang. 2010. A Molecular View of the Cholesterol Condensing Effect in DOPC Lipid Bilayers. J. Phys. Chem. B. 114: 7516–7523.
22. McConnell, H.M. 1991. Structures and Transitions in Lipid Monolayers at the Air-Water Interface. Annu. Rev. Phys. Chem. 42: 171–195.
23. http://stackoverflow.com/questions/28567166/uniformly-distribute-x-points-inside-a-circle